Multifunctional PLGA-PFCE Nanoparticles: A Versatile Platform for Imaging and Therapeutic Applications via SPAAC Functionalization

Prepared by:

Marjan kalati

Supervised by:

Alvja Mali, Ezgi Basavci and Mangala Srinivas

Master biotechnology, medical specialization

Wageningen University and Research

Cell biology and Immunology

October 2024

Contents

1 Introduction

Magnetic resonance imaging (MRI) is widely used in clinical and preclinical imaging, often relying on contrast agents (CAs) to enhance signal intensity and improve visibility. [1] However, many traditional CAs face limitations, including complex localization and potential toxicity at high concentrations. Localization is challenging due to the strong background signals from water and natural tissue contrasts, such as blood clots and endogenous iron. This low sensitivity often necessitates higher concentrations of CAs, which increases the risk of toxicity.[2]

To address these challenges, Fluorine-19 can be used as an alternative nucleus to be detected, rather than the proton.[3] This method employs perfluorocarbons (PFCs) as a ^{19}F source for MRI. PFCs are characterized by their strong fluorophilicity and lack of affinity for both hydrophilic and lipophilic environments, exhibiting both hydrophobic and lipophobic properties.[4] Perfluoro-15-crown-5-ether (PFCE) is particularly suited for ^{19}F MRI because it produces a single, sharp spectral peak due to the magnetic equivalence of all fluorine-19 atoms in its structure.[5]

Encapsulating PFCs into nanocarriers such as lipid- or polymer-based systems can improve their performance. PLGA (poly(lactic-co-glycolic acid)) is the most commonly used polymer for encapsulation due to its biocompatibility, biodegradability, and FDA approval. Although PLGA-based NPs are often described in the literature[6] as having a core-shell structure, recent studies have shown that PLGA-PFCE NPs can have a multicore internal structure.[7] This multicore design offers advantages, such as improved colloidal stability, solubility, and faster clearance from internal organs. This structural difference is key to reducing retention time and making the NPs more suitable for various applications.[7][8] In addition, the multicore structure requires careful control of synthesis parameters to encapsulate PFCE effectively.[9]This sensitivity means that any modifications made during the synthesis could compromise the PFCE encapsulation and multicore structure. As a result, functionalization of the NPs can be performed post-formulation, ensuring that the multicore remains intact while enabling further modification for targeted applications.

Targeting NPs enhances the specificity and effectiveness of both diagnostic and therapeutic applications.[10] These nanoplatforms are designed to target specific molecules, enabling early detection and precise treatment.[11] Additionally, PFC NPs are valuable for monitoring drug delivery,[12] tracking cells,[13][14] and visualizing drug distribution.[15][16] Strategies for promoting NP accumulation in tissues or cells involve passive and active targeting. Passive targeting increases NP retention in the bloodstream by modifying nanocarriers but lacks specificity, making it difficult to reach the target tissue.[17][18] Active targeting addresses this by attaching specific ligands, such as antibodies, peptides, or other biomolecules, to the NPs. These ligands bind to receptors on target cells, enhancing specificity and uptake.[18] [19] This approach not only improves delivery but also allows real-time monitoring of therapeutic responses using imaging agents.[20]

Since active targeting offers greater specificity than passive targeting, this study focuses on this strategy. Active targeting requires careful design of the NP surface to ensure specific ligand binding. Several techniques can be employed to modify the NP surface, including lipid coating,[21]albumin coating,[20] polysaccharide-based coating,[22] and PEGylation surface modification. Among the available techniques, we chose polyethylene glycol (PEG) as a linker and it is one of the most widely adopted approaches. PEG serves as a functional bridge between the NP and the targeting ligands, facilitating the attachment of biomolecules such as antibodies, peptides, or other active agents that bind to specific cell receptors.[23] Moreover, the flexible and hydrophilic structure of PEG allows it to extend NPs surface, creating sufficient space for attached ligands to interact effectively with their target receptors. [24] In addition to facilitating ligand attachment, PEG helps prevent nonspecific binding to cells and proteins in the bloodstream, reducing the immune system detection and clearance. This leads to longer circulation time for the NPs, increasing the chances of reaching their intended target.[25] This versatile role makes PEG an important component for designing NPs that are both stable and highly specific for targeting.[26]

After incorporating PEG as a linker, choosing an appropriate technique is important for attaching targeting ligands to the PEGylated NP surface. Several widely used techniques offer different advantages based on the specific requirements of the targeting process. One common method is carbodiimide chemistry, which typically involves EDC/NHS coupling. This approach forms covalent bonds between carboxyl and amine groups, making it useful for conjugating proteins, peptides, or antibodies to the NP surface.[27] Another method is the maleimide reaction, which is particularly effective for attaching thiol-containing ligands to maleimide-functionalized NPs, offering high specificity and efficiency for certain types of biomolecules.[28] Electrostatic interactions provide a simpler, non-covalent approach, using the attraction between oppositely charged particles to bind ligands to NPs. While this method is less stable than covalent bonding, it can be useful in some targeting applications. [29]

Among these options, click chemistry stands out due to its high selectivity, efficiency, and ability to proceed under mild conditions. This technique enables the rapid and specific formation of covalent bonds between azide- and alkyne-functionalized molecules, ensuring strong, stable attachment of targeting ligands. Additionally, click chemistry is versatile and compatible with various biomolecules, making it an excellent choice for designing NPs with precise and robust ligand binding. [27] [30] [31]For our study, we selected click chemistry for its reliability in producing stable conjugations, maximizing the effectiveness of active targeting.

Examining the various types of click reactions commonly used in NP surface modification is essential for optimizing ligand attachment. The copper(I)-catalyzed azide-alkyne cycloaddition (CuAAC) is widely recognized for its high efficiency and selectivity. However, its application in biological systems is limited due to potential copper ion toxicity.[32] [33] [34] To overcome this challenge, alternative click chemistry variants have been developed. Strain-promoted azide-alkyne cycloaddition (SPAAC), a copper-free version, has emerged as a safer alternative suited for in vivo applications. This method

employed the intrinsic ring strain of cyclooctyne compounds to facilitate the chemical process, thereby eliminating the requirement for potentially toxic copper-based catalysts.[35][36] Another click chemistry variant is the thiol-ene reaction, which enables efficient conjugation between thiol and alkene groups. However, its practicality is limited in certain biological contexts because it often requires the use of photo-initiators or radical initiators, which can potentially damage sensitive biomolecules.[37]

In our approach, we particularly employed SPAAC click chemistry due to its high specificity, mild reaction conditions, and low risk of cross-reactivity.[38] This method has been successfully utilized in a range of biological applications, including radioisotope labeling,[39] [40] live-cell imaging,[41] and surface modification. [42] In our design, the SPAAC reaction facilitates the conjugation of targeting ligands through the interaction between dibenzocyclooctyne (DBCO) and azide-tagged molecules, forming stable triazoles. The stability of both the DBCO and azide groups ensures the long-term structural integrity of the NP-ligand complex. Notably, this reaction is highly specific, as azides react exclusively with DBCO even in the presence of functional groups like amines ($-NH_2$), thiols (-SH), and carboxyls (-COOH).[43] This bioorthogonal reaction allows for precise and controlled ligand attachment, making it ideal for our two-step targeting strategy involving PEGylation by PEG-DBCO followed by click chemistry to achieve effective active targeting.

This study introduces a promising platform for targeted molecular imaging using PLGA-PFCE NPs, employing bioorthogonal SPAAC reactions for versatile target binding. To achieve effective active targeting, we designed the NPs with a two-step strategy: first, the use of PEG as a linker, facilitating ligand binding; and second, click chemistry for precise ligand attachment. We optimized click chemistry conditions, specifically focusing on DBCO concentration, reaction time, and temperature to enhance conjugation efficiency while maintaining the stability of the multi-core PFCE-encapsulated PLGA NPs, as described in the literature.[7] [8] Unlike other methods, our approach required maintaining the multi-core NPs formulation, which is essential for effective ^{19}F MRI imaging. The PFCE content is crucial for imaging performance, yet challenging to work with due to its low affinity for PLGA and non-hydrophobic nature. Therefore, our adjustments in functionalizing the NPs after PFCE entrapment were critical, as significant material loss was predicted during the process. These optimizations ensured the successful preparation of functional NPs, enabling precise targeting through bioorthogonal click chemistry reactions with azide-tagged dyes and peptides.

2 Method and Material

2.1 Chemical and Reagents

All chemicals listed were used without further purification. The following chemicals were purchased from Sigma Aldrich: Deuterium oxide (D2O), Dimethyl Sulfoxide-d6 (d-DMSO), Poly(vinyl alcohol), trifluoroacetic acid (TFA), and Azide-fluor 488 (AF-488). Dichloromethane (DCM) was obtained from EMSURE, Merck Millipore (Darmstadt, Germany). PEG linkers (DBCO-NHCO-PEG4-amine) were acquired from Broad Pharm. Thermo Scientific supplied N-hydroxysuccinimide (NHS), 1-(3-dimethylaminopropyl)-3-ethylcarboiimide hydrochloride (EDC), and BupH™ MES Buffered Saline Packs. Sephadex G-50™ Superfine was purchased from Cytiva, and Perfluoro-15-crown-5-ether (PFCE) was obtained from Exfluor Research Corporation. TAT-Lys(N3)-6-FAM was custom-synthesized by Marco Neves at the University of Barcelona. Poly(lactic-co-glycolic acid) (PLGA) and distilled triethylamine were previously synthesized in-house. Spectra/Por 6 Dialysis membranes (15 kDa MWCO) were purchased from Spectrum™. Ultrapure water was obtained using a Purelab Chorus Elga filtration system.

2.2 PLGA-PFCE nanoparticles (NPs) preparation

PLGA NPs encapsulating perfluro-15-crown-5-ether (PFCE) were prepared by using a single oil-in-water emulsion. The whole process is depicted in Figure 1. Briefly, PFCE was encapsulated by dissolving PLGA in 3 mL of dichloromethane (DCM) and mixed with PFCE by pre-sonication or pipetting up and down with a glass pipette. The resulting double-phase liquid was added to a solution of 2% poly (vinyl alcohol) (PVA) while sonication was started. The entire mixture was sonicated on an ice water bath for 3 minutes. After sonication, the DCM was evaporated while stirring at 4˚C overnight. Afterward, the NPs were washed 3 times by centrifugation and the supernatant was replaced with Milli-Q (MQ) water (10 ml). After the last wash, the particles were resuspended in 5 ml MQ water, frozen with liquid N_2, and freeze-dried for 48 hours. The resulting dry powder was stored in the freezer at -20˚C for further experiments.
The protocol was modified to optimize PFCE encapsulation in PLGA and enhance PEGylation efficiency. After the final washing step, the NPs were resuspended in 5 ml of MES buffer to achieve a concentration of 20 mg/ml. Of this suspension, 4 ml were retained in liquid form for PEGylation, while 1 ml was kept to facilitate characterization via DLS and zeta potential measurements.

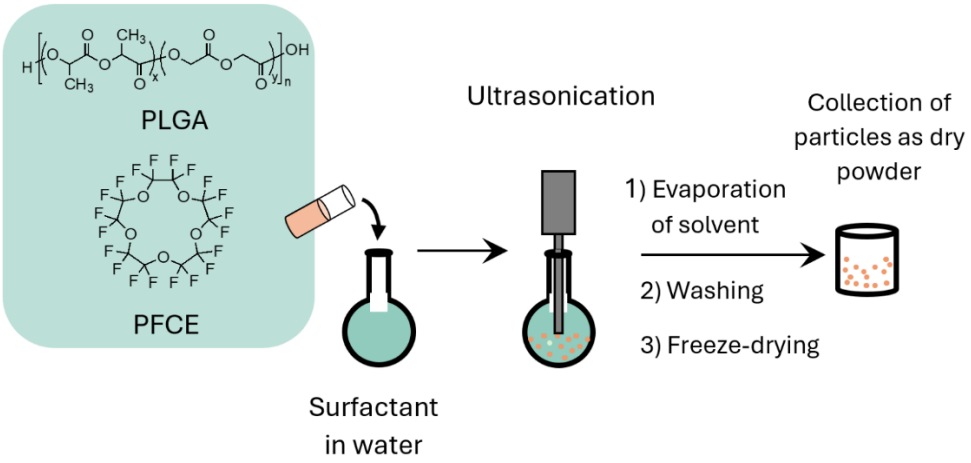

Figure 1: *Step-by-step protocol to produce NPs*

2.3 PLGA-PFCE NPs Characterization

Characterization in research refers to the process of describing and analyzing the properties and features of materials, compounds, or systems to understand their behavior, structure, and composition. Characterization of PLGA-PFCE NPs involves various techniques to determine the properties and behavior of PLGA-PFCE NPs, including measuring particle size, polydispersity index, zeta potential.

2.3.1 Dynamic Light Scattering (DLS)

For the size and charge investigation of the particles, DLS was performed on a Malvern Zetasizer ZS at a scattering angle of θ = 173° using disposable cuvettes. The NPs were solubilized in MQ water with a concentration of 10 mg/ml. The stock was diluted 100 times with a final volume of 1 ml. The dilution was added to plastic cuvettes, and the ζ-potential and diameter of the particles were measured. The final diameter of each sample is reported as an average of 4 measurements of each 6 runs of 10 seconds (at 21 °C).

2.3.2 Nuclear Magnetic Resonance (^{19}F and ^{1}H NMR)

^{19}F Nuclear Magnetic Resonance (NMR) was used to check the PFCE content. For ^{19}F NMR, approximately 5 mg of NPs were resuspended in 500 µl of D2O. 100µl of 1% trifluoroacetic acid solution was added to the sample as an internal standard. The spectrum was measured on a Bruker Avance III 400MHz NMR spectrometer with 8 scans, with each a 25-second delay.
For ^{1}H NMR, ±5 mg of NPs was resuspended in 500 µl of d-DMSO. DMSO is often used to avoid interference from solvent protons in the analysis of hydrogen-containing compounds. This is because the technique is based on the magnetic resonance of hydrogen nuclei, and any extra protons in the solvent could disrupt the structure prediction. The spectrum would then be measured on a high-resolution NMR spectrometer, the Bruker 700MHz instrument.

2.4 PLGA-PFCE NPs surface modification

PEG molecules were attached to the PLGA surface for further modification after the NPs were formulated. This was done via a two-step coupling using 1-(3-dimethylaminopropyl)-3-ethylcarboiimide hydrochloride (EDC) and N-hydroxy succinimide (NHS) (Figure 2).

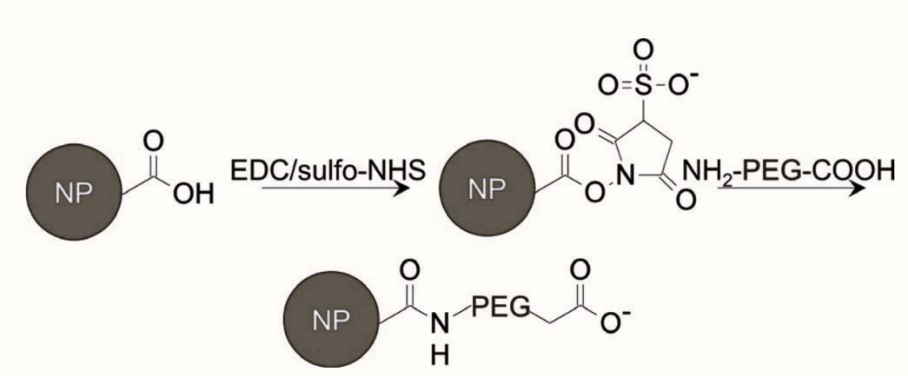

Figure 2: *EDC-NHS reaction to bind PEG to surface NP [44]*

2.4.1 Optimization of PEG4-DBCO surface PEGylation on PLGA-PFCE NP

The PLGA NPs (80mg, 0,0057 mmol) were solubilized in MES buffer (8ml,10 mg/ml, pH 5-6) to deprotonate the carboxyl group on the surface of the particles. The process was adjusted by taking 4 mL of stock NPs sample solution with a concentration of 20 mg/mL, which corresponds to 80 mg of the dried sample. After that, 4 mL of MES buffer was added to reach a final volume of 8 mL. To the deprotonated NPs, eight times the molar excess of EDC (8.8 mg, 0,045 mmol) was added. Immediately after, a ten times molar excess of NHS (6.6 mg, 0,057 mmol) was added, to react with the formed unstable ester. This mixture was left to react for two hours while stirring, without light, and at RT. The PEG4-DBCO (182µl, 100 mg/ml, 637,6 g/mol) molecules with five times the molar equivalent of NPs were added after raising the pH to ~8 with 75 µl triethylamine. The mixture was left to react overnight without light while stirring (RT).
To wash away the unbound molecules, the reaction mixture was put into pre-wetted regenerated cellulose tubing with a molecular weight cut-off of 15 kDa .First, the membrane was active in warm MQ water and then it was closed with clips and placed into a large beaker for 3 days of dialysis, the first day with PBS 1x and the last 2 days with MQ water. At a minimum, the solution was changed 2 times every day. On the last day, the sample with the PEGylated NPs was taken out of the membrane, frozen with liquid N_2, and freeze-dried for 48 hours. Following this, the samples were characterized by DLS and ^{1}H NMR as detailed in sections 2.3.1 and 2.3.2 respectively.

2.4.1.1 PEGylation yield calculation by UV-Visible

A standard curve was made based on different concentrations of PEG to calculate the PEGylation yield. UV-Vis spectroscopy was performed, using a SpectraMax iD3 plate reader and Greiner 96 well plate flat transparent, with PEG4-DBCO measured at a wavelength of 290 nm. To determine PEGylation efficiency, first batches were prepared with known concentration, and then the UV-Vis absorbance of each batch was measured at 290 nm. An equation derived from the standard curve was used to calculate the concentration of PEGylated NPs (PNPs) based on their UV-Vis absorbance. Subsequently, the PEGylation efficiency was calculated by dividing the measured concentration from the UV readings by the prepared (known) concentration and multiplying by 100. This method, using UV-Vis spectroscopy and a standard curve, allows for quantifying PEGylation yield.

$$PEGylation\ efficiency(\%) = \left(\frac{Measured\ concentration\ from\ UV}{Prepared\ concentration}\right) \times 100$$

Equation 1: *PEG4-DBCO efficiency*

2.5 SPAAC Click reaction with Dye and TAT-peptide

PEGylated NPs with terminal DBCO groups were functionalized using SPAAC. The moles of DBCO on the NPs were first calculated based on the PEGylation efficiency. Then, using a 2:1 molar ratio (2 moles of DBCO to 1 mole of dye or peptide), the required amount of dye/peptide was calculated. Additionally, the concentration of the reaction was maintained between 1 to 2 mg/ml. For instance, the PNPs (10 mg) with a DBCO efficiency of 24.3%, were dispersed in 5 mL of 1x PBS. Subsequently, 50 µL of a stock solution of AF488 at 1 mg/mL concentration was added to have a 2:1 mol ratio. The mixture was allowed to react for two hours under continuous stirring, in the dark, and at RT. Following the reaction, the solution was washed twice with MQ by centrifugation at 17,000 RCF for 30 minutes at RT to remove unbounded dye. Then it was frozen using liquid nitrogen and freeze-dried for 48 hours. To optimize the reaction, varying molar equivalents of Azide-fluor 488 were added to the NP suspension.

After optimizing the reaction for the dye, the same procedure was repeated for TAT-Lys(N3)-6-FAM, a cell-penetrating peptide labeled with 6-carboxyfluorescein (6-FAM) and modified with an azide group. This allowed for the evaluation of the SPAAC reaction efficiency with a biologically relevant molecule under the same conditions as the Azide-fluor 488 experiments. The peptide conjugation followed the optimized conditions established in the dye experiments. The only modification to the procedure was due to the higher molecular weight of the peptide, requiring an adjustment in the amount of TAT added to keep a 2:1 mol ratio.

2.5.1 Click reaction characterization by exclusion chromatography (SEC)

The conjugation efficiency for the SPAAC reaction was determined using SEC. It is primarily used to separate molecules based on their size. In this experiment, a Chromatography column (Lenz Laborglasinstrumente™ 05450703 from Fisher Scientific) was loaded with around 3 mg of G50 Sephadex gel eluent in 40 ml PBS1x for several minutes. Then, the SPAAC reaction sample was run to the column. Fractions

were collected as they eluted from the column, with most fractions being collected in 3 ml volumes, except for fractions 1 and 2, which were collected in 5 ml and 4 ml volumes, respectively. The absorbance was measured at 494 nm using a UV-VIS spectrum analyzer (SpectraMax iD3), which is used in section 2.4.1.1.

2.5.2 Click reaction characterization by DLS

Following SEC, the collected fractions were divided into two groups: the initial fractions and the later fractions. Each group was analyzed using DLS to determine the hydrodynamic size and count rate (kps) of the particles. This analysis provided insights into the presence of NPs versus free dye or peptide

2.5.3 Click reaction characterization by Fourier Transform Infrared (FT-IR)

FT-IR spectroscopy was employed to characterize the click reaction and confirm its occurrence. Spectra were recorded using a Bruker Tensor 27 FT-IR spectrometer. Solid samples were prepared by finely grinding a small amount of each sample and then pressing it into thin, transparent pellets. After that, Spectra were collected in the range of 4000-400 cm^{-1} with high resolution. Three samples were analyzed: the TAT peptide, PNPs, and the reaction mixture after the click reaction, which were dried. By overlaying the FT-IR spectra of these samples, it was possible to identify any peak, indicating the success of the reaction. While FT-IR spectroscopy provided valuable insights into the functional group changes during the reaction, complementary analysis using ^{1}H NMR spectroscopy is recommended for a more comprehensive characterization of the reaction products and to fully validate the results.

2.5.4 Click reaction characterization by ^{1}H-NMR

^{1}H-NMR is similar to the procedure described in section 2.3.2

2.6 Click reaction yield calculation by Absorbance

To determine the click reaction yield, a standard curve was created using various concentrations(µmol) of azide-fluoro 488 (λex = 494 nm) and measuring their absorbance. First, batches of click reaction samples with a known concentration(mol) of DBCO were prepared. After SEC, the absorbance of all collected fractions was measured using UV-Vis spectroscopy at 494 nm. The first 10 fractions, representing DBCO bound to dye, were summed. By using the equation from the standard curve, the concentration of DBCO bound to dye was calculated. The final click reaction yield was determined by dividing this calculated concentration by the initial prepared concentration of DBCO and multiplying by 100, giving the percentage yield after SEC efficiency.

2.7 Cell Culture

HeLa-80 cells were cultured in a complete Dulbecco's Modified Eagle Medium (DMEM) supplemented with 10% fetal bovine serum (FBS) and a combination of

penicillin-streptomycin (100 units/mL penicillin and 100 µg/mL streptomycin). The cells were incubated at 37°C in 5% CO2. HeLa-80 cells were subcultured until they reached approximately 85% confluency, then cells were washed with PBS and detached with 0.25% Trypsin/EDTA solution.

2.8 Cell uptake and cell viability with flow cytometry

For flow cytometry analysis, HeLa-80 cells were seeded at 100,000 cells per well in a 24-well plate. Three sample types were prepared: NPs alone, NPs conjugated with AF 488 via click chemistry and NPs conjugated with TAT peptide via click chemistry. Each sample was prepared at a concentration of 10 mg/ml in PBS, and 0.5 mg was added to each well. The cells were washed once with PBS to remove media, and 0.5 ml trypsin (diluted 1:2 in PBS) was added to detach the cells, followed by incubation at 37°C for around 5 min. Once the cells were detached, an equal volume of complete media was added to neutralize the trypsin, and cells were collected in pre-labeled tubes. The samples were centrifuged at 600g for 5 minutes at 4°C, and the pellets were resuspended in 200 µL of PBS containing Zombie UV^{TM} Fixable viability dye (prepared by diluting 1 µL of stock solution in DMSO per 0.5 mL of PBS). Cells were gently vortexed and incubated in the dark at room temperature for 15-20 minutes. After incubation, the cells were centrifuged at 600g for 5 minutes at 4°C, and washed with PBS.
Following that, cells were washed three times with PBS, with the final wash performed in a smaller volume (200-500 µL depending on the cell count). The samples were then transferred to a 96-well plate, with each sample distributed across three wells, and gently pipetted to ensure uniformity before proceeding to flow cytometry analysis.

Flow cytometric analysis was performed using a Cytoflex LX instrument. The first step involved gating the viable single-cell population on a forward scatter (FSC) versus side scatter (SSC) plot, which excluded cellular debris and cell aggregates. Subsequently, the fluorescence intensity of the gated single-cell population was measured using the FITC channel. The resulting data were visualized as a histogram and further analyzed using FlowJo software.

2.9 Confocal Microscopy

HeLa-80 cell lines were used for the cell uptake studies *in vitro*. The cells were cultured in a humidified chamber at 37°C and 5% CO_2 one week before the experiments for pre-conditioning, in DMEM supplemented with 10% FBS, 100 U of penicillin and 100 µg/mL streptomycin. The cells were plated one day before the uptake experiment in eight-well LabTek Chamber Slides (Nunc, Langenselbold, Germany) and particles were added at time zero at 5 mg NP/million cells. At different measuring timepoints, the particles were washed 3x with PBS and Hoescht EasyProbe (ABP Biosciences, Beltsville, USA) was applied for 15 min to stain the nuclei. Finally, the remaining dye was washed and the samples were fixed for 20 minutes with PFA 4% and re-filled with PBS. Leica TCS SP8 X White Light Laser inverted confocal microscope (Leica Microsystems B.V., Amsterdam, Netherlands) was used for imaging, with an HCX PL APO 40×/1.4 NA dry objective and LasX software for image processing. The imaging settings were kept constant between

samples and the same post-processing method was applied for the analysis. The images shown are 3D reconstructions using the maximum intensity projection method. Nuclei are depicted in blue, particles in green, and bright-field in greyscale.

3 Results and Discussion

The functionalization of NPs is key to enhancing their specificity and effectiveness for biomedical applications, particularly in targeting specific organs, cells, or tissues.[45] This process enables precise attachment of targeting ligands to NP surfaces, facilitating active targeting that promotes efficient delivery, reduced non-targeted effects, and enhanced imaging contrast.[46][47] Additionally, functionalization improves biocompatibility, increases stability in physiological environments, and allows for the integration of multiple functionalities—such as therapeutic agents and imaging capabilities—onto a single NP platform.[48]In this study, post-formulation functionalization of PLGA-PFCE NPs was employed to preserve the integrity of their multicore structure, a key feature for ^{19}F MRI performance.

To achieve this, we developed and characterized PLGA-PFCE NPs functionalized with DBCO to facilitate bioorthogonal click chemistry. First, we used carbodiimide chemistry to conjugate PEG-DBCO to the surface of the NPs. This method involves activating the carboxyl groups on the NPs surface with a carbodiimide reagent, such as EDC, in combination with NHS. The EDC activates the carboxyl groups, while NHS stabilizes the reactive intermediate, increasing the efficiency of the coupling reaction. This activation step enables covalent bond formation with the amine groups of PEG-DBCO, resulting in stable covalent attachment to the NPs.[44]

Subsequently, the click reaction process involved installing two mutually reactive functional groups: the strained alkyne, which is incorporated into DBCO and linked to the NPs via a PEG linker, and the azide group, which is conjugated to either the dye used as a model or to a peptide. The PEG-DBCO enables efficient attachment to the NPs, while the azide-functionalized dye or peptide serves as the reactive counterpart in the click reaction. Fluorophores were incorporated to allow real-time monitoring of the reaction without interfering with the functionalization process.

This study demonstrates the synthesis, optimization, and in vitro evaluation of these functionalized NPs for potential imaging applications. We detail the preparation and characterization of the NPs, forming the foundation of our study. Following this, we discuss the process of linking PEG-DBCO to the NPs, a critical step in enhancing their functionality. We then detail our efforts to optimize the click chemistry conditions, focusing on maximizing bioconjugation efficiency. Finally, we present an analysis of the NPs' in vitro performance, demonstrating their potential for practical applications in molecular imaging.

PLGA-PFCE NPs & PLGA-PEG-DBCO NPs characterization

All synthesized NPs batches were characterized to determine their size, polydispersity index (PDI), and weight percentage of encapsulated PFCE. The NPs exhibited PDI values below 0.3, indicating uniform size distribution [49], and particle diameters within the ideal range of 180-200 nm. [50] DLS confirmed the successful synthesis of the NPs. The PFCE encapsulation was quantified using ^{19}F NMR spectroscopy, with an average of 10-15 wt% across 10 batches (Table 1). Initially, we focused more on the chemical aspects of the NPs system, which led to inadequate optimization of PFCE encapsulation. However, batches that were specifically optimized for PFCE content demonstrated significantly higher encapsulation efficiencies.

Table 1: *the average Size, PDI, PFCE %, and PEGylation efficiency*

Sample	Size(nm)	PDI	PFCE (wt%)	PEGylation Efficiency (%)
NPs(average of 10 samples)	186.0 ±1.8	0.11 ± 0.005	11.5± 2.4	N/A
PNPs(average of 10 samples)	190.5±2.1	0.08±0.007	N/A	21.6± 8.5

To optimize PFCE encapsulation and reduce losses during lyophilization, we modified the process to reduce the number of freeze-drying steps. Normally, NPs are freeze-dried after encapsulation, followed by PEGylation and a second round of freeze-drying. In this study, we adjusted the method by PEGylating the NPs directly without an intermediate freeze-drying step. This modification aimed to minimize PFCE loss and simplify the process.

We designed an experiment where the NPs were PEGylated first, followed by a single round of freeze-drying to obtain a powder. This batch was then split into two groups: one proceeded through a click reaction and was freeze-dried again to produce a powder for in vitro use, while the other was stored in 1x PBS instead of being dried. The schematic workflow is shown in Figure 3.

DLS and ^{19}F NMR were performed after the initial lyophilization to assess the PFCE encapsulation efficiency. As shown in Figure 4A, the results indicated that PFCE encapsulation efficiency decreased by about 10% after two rounds of freeze-drying. Therefore, to preserve PFCE content for further experiments, it is preferable to store the NPs in liquid form (PBS). However, if PFCE retention is not critical, the powder form can still be used for other studies.

Additionally, we monitored the size and PDI of the liquid-stored NPs over three days to evaluate their stability, as shown in Figures 4B-C. The NPs were stored at 4°C, and the DLS data revealed that the particle size remained relatively stable over the 72 hours (Figure 4B). The PDI also remained consistent, indicating that the size distribution of the NPs did not significantly widen (Figure 4C). These findings suggest that the NPs stored

in liquid form are stable for at least three days, though further experiments are recommended to assess long-term stability. This observation aligns with a study that demonstrated the stability of PLGA NPs, showing that they remained colloidally stable in aqueous buffers for over two weeks. [51]

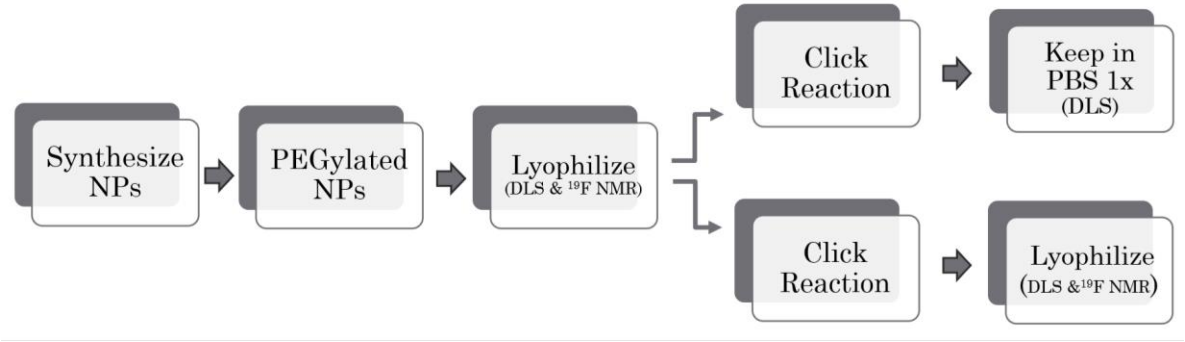

Figure 3: *Schematic representation of NP synthesis and modification workflow.*

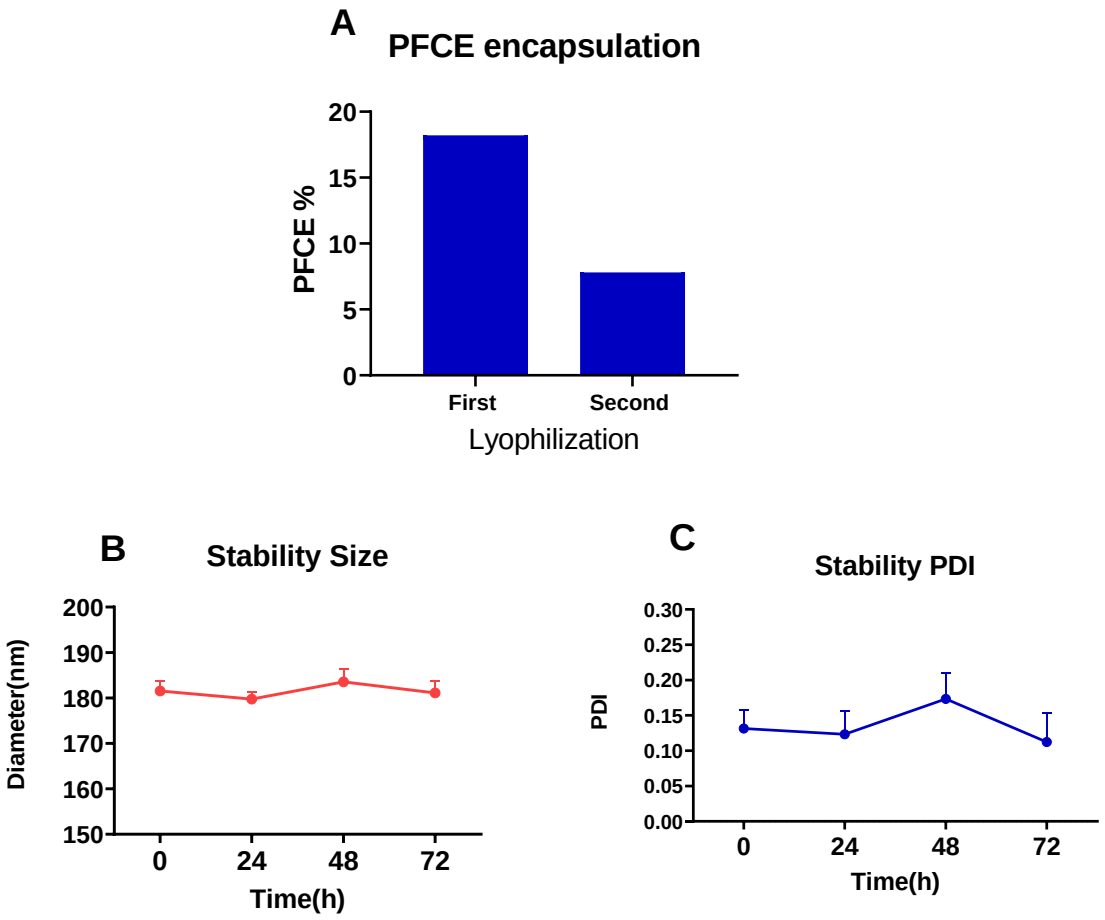

Figure 4: *This figure summarizes the results of PFCE encapsulation efficiency and the stability of NPs over time. A) PFCE encapsulation efficiency after the first and second lyophilization rounds. B) NP size measured over 72 hours to assess stability in liquid form. C) PDI measured over 72 hours, reflecting the distribution of particle sizes during storage.*

To confirm the presence of PEG-DBCO on the NP surface, ^{1}H NMR spectroscopy was employed (Figure 5). The spectrum of PNPs showed peaks corresponding to the PLGA matrix at 1.5, 4.8, and 5.2 ppm, labeled as A, B, and C in Figure 5, respectively. [52]Additionally, residual PVA surfactant post-washing appeared around 4-5 ppm, specifically at 4.6, 4.4, and 4.2 ppm. [53] The PEG4-DBCO was also identified, with the PEG hydrogen atoms producing a small peak at 3.44 ppm. This peak is relatively small due to the short PEG4 chain, which only has four repeating units. The aromatic protons of DBCO appeared as multiple peaks between 7.1-7.9 ppm, highlighted in the zoomed-in rectangle. These peaks have low intensity, consistent with the approximately 20% PEGylation efficiency.[54][55] The PFCE molecule is not observable in the ^{1}H NMR due to the absence of protons for visualization.

The efficiency of PEGylation was quantitatively determined using a standard curve based on DBCO absorption. UV-Vis spectroscopy was performed, with PEG4-DBCO measured at a wavelength of 290 nm and the resulting data are presented in Table 1. [55]

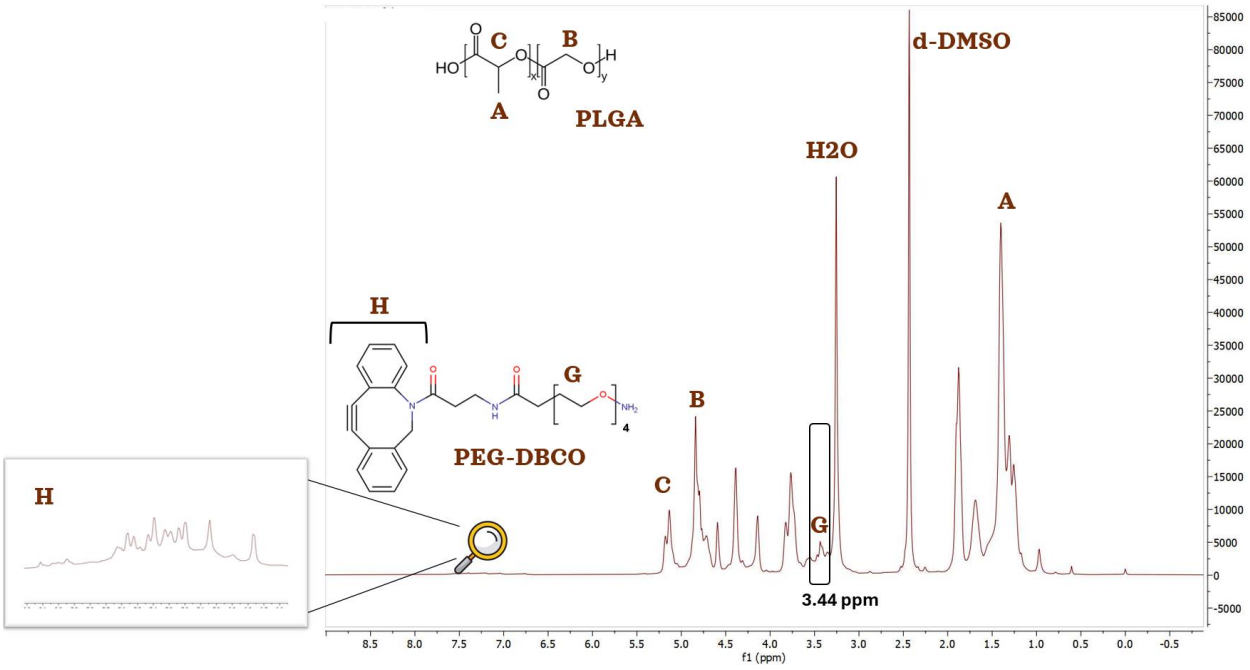

Figure 5 : *^{1}HNMR result for the PEG4-DBCO PLGA NPs*

Click Chemistry Optimization and Efficiency

After NPs synthesis and characterization which was followed by PEGylation, we aimed to optimize the conditions for the click reaction, particularly focusing on achieving an efficient ratio of DBCO on NPs surfaces and the amount of Azide-Fluor 488(λex/em = 494/517 nm) and TAT-Lys(N_3)-6-FAM peptide(λex/em = 498/530 nm). This optimization was crucial because it directly influenced the efficiency and specificity of the click reaction. A well-optimized DBCO-to-azide ratio ensures maximal reaction efficiency, which is essential for achieving high yields of the desired conjugates. [56]

Furthermore, the reaction conditions, including time and temperature, were varied to identify the most effective parameters for the click reaction. Time is a key factor in click chemistry, as it can significantly affect the reaction kinetics and the extent of conversion to the desired product. Prolonged reaction times may lead to increased yields, but they can also result in side reactions or degradation of sensitive components.[57] Temperature plays a similar role; higher temperatures can accelerate reaction rates but may also promote unwanted side reactions or affect the stability of the NPs.[58] By adjusting these parameters, we focused on establishing the most effective conditions for our click chemistry reaction.

The DBCO mentioned here refers to the amount bound to the NPs surfaces, as determined from previous calculations for PEGylation efficiency. We first utilized SEC to identify the elution profiles of bound NP-dye complexes and free dye by analyzing their separation patterns. This approach allowed us to determine the specific fractions containing the bound complexes. Subsequently, we focused our analysis on these binding sites. Based on SEC analysis, larger DBCO-functionalized NPs pass through faster (fractions 1−10), while the free Azide-Fluor 488 (AF-488) dye was detected in fractions 12-30. [42] Figure 6 shows 2:1 DBCO to dye ratio produced higher absorbance in the bonded fractions compared to a 3:1 ratio, with the amount of free dye remaining constant across both ratios (Figure 6A-B). The dye concentration was not increased relative to DBCO, because Figure 6A shows that unreacted dye remained in the reaction mixture. This suggests that a 2:1 DBCO to dye ratio achieves more efficient conjugation. The increased efficiency at this ratio could be related to reduced steric hindrance and improved accessibility of the reactive DBCO sites on the NP surface. This optimal ratio likely provides an ideal spacing where DBCO molecules are sufficiently distributed, minimizing molecular congestion at the NPs binding sites. The lower density of DBCO groups may decrease obstruction between adjacent molecules which allows them to be more exposed and accessible for reaction with the dye. Consequently, this arrangement facilitates more efficient conjugation. This interpretation aligns with the research of Idiago-López et al. [59] They focused on using bioorthogonal chemistry for attaching magnetic NPs (MNPs) to living cell membranes.

The presence of free dye across different DBCO-to-dye ratio highlights the key role of DBCO availability and accessibility in influencing reaction efficiency. This finding was supported by previous research on surface functionalization strategies, which emphasize the importance of optimizing reactive group density and accessibility for improved conjugation outcomes.[60][61]

After having assessed the adequate molar ratio between the dye and the DBCO, we moved to the time and temperature. [57] [58] These parameters were changed to determine the optimal conditions for the click reaction between DBCO-functionalized NPs and AF-488. Interestingly, our results showed no significant difference in conjugation efficiency between 2-hour and 24-hour reaction times (Figure 6B).[42] Similarly, we observed no notable difference in reaction outcomes when comparing room temperature conditions to 37°C (Figure 6C). These indicate that the click reaction proceeds efficiently and reaches completion relatively quickly, even under mild conditions.

Unlike simpler solution-phase reactions, the steric hindrance and restricted mobility of reactive groups (e.g., DBCO on the NPs surface and azide on the target molecule) reduce the probability of successful encounters in a PLGA NPs system.[62] [63] Considering these limitations, we established a minimum reaction time of 2 hours to ensure sufficient interaction between the reactive groups and optimize the conjugation process. Our observations align well with the work of Bouvet et al,[64] who demonstrated the rapid and efficient nature of SPAAC reactions for ^{18}F-labeling. In their study, they achieved high radiochemical yields (70-90%) within just 5-15 minutes at room temperature. This remarkable speed and efficiency confirm our findings of rapid reaction completion, even at room temperature.

The lack of temperature dependence suggests that the reaction kinetics are not significantly influenced by temperature changes, which is typical for SPAAC due to its high intrinsic reactivity and energy release upon cycloaddition.[65] These studies are further supported by the study on live monitoring of SPAAC using inline ATR-IR spectroscopy. The researchers were able to monitor SPAAC reactions at various temperatures, ranging from 0 to 60°C, demonstrating the flexibility of the reaction across a wider temperature range. They observed that while reaction rates did increase with temperature, efficient cycloaddition still occurred even at lower temperatures. [66]

In the final optimization phase, our study focused on varying the amount of DBCO on NP surfaces while maintaining a constant 2:1 ratio between DBCO and AF-488. The results demonstrated a clear correlation: as we increased the DBCO concentration on the NP surface while maintaining the 2:1 ratio of DBCO to dye, we observed higher absorbance values in the conjugated fractions. This increase in absorbance directly indicates an improvement in conjugation efficiency (Figure 6D).[67] This improvement can be

attributed to the increased probability of successful reactions between DBCO and the dye at higher DBCO concentrations, resulting in more efficient binding.

While this trend aligns with findings from Perez et al. [42] our approach differs from previous studies in a significant way. We focused on optimizing DBCO density on solid NPs rather than adjusting mole percentage in nanoemulsions. This distinction is crucial as it allows for more precise control over the surface chemistry, potentially leading to better targeting and functionalization outcomes.[68]

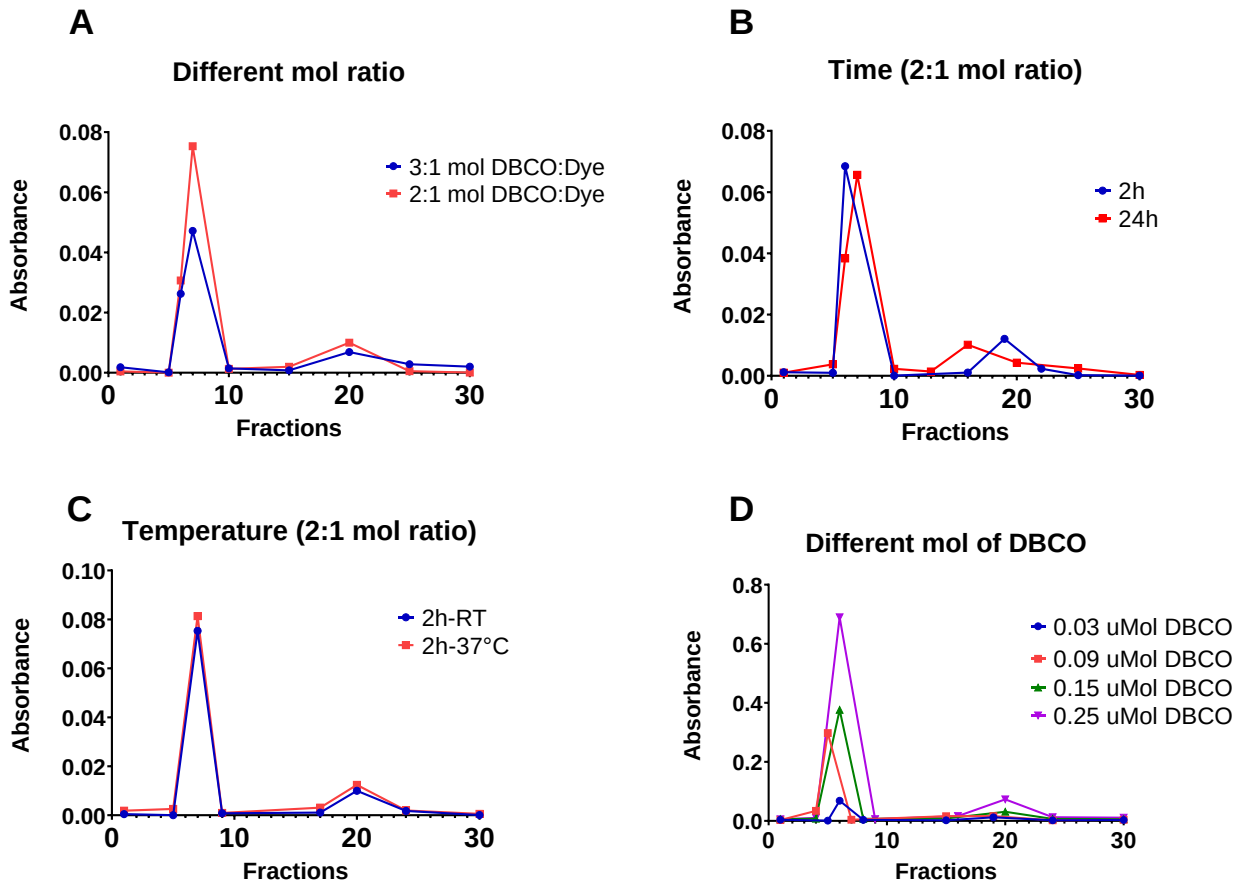

Figure 6: *A) Comparison of absorbance for two different molar ratios of DBCO to dye (3:1 and 2:1) across various fractions. B) Absorbance was measured after 2 hours (blue) and 24 hours (red) at room temperature (RT). C) Absorbance comparison between samples incubated for 2 hours at room temperature (blue) and 2 hours at 37°C (red).D) Absorbance for different concentrations of DBCO in a 2:1 mol ratio of DBCO to dye across fraction numbers.*

To quantify the efficiency of the click reaction, we analyzed the first 10 fractions from SEC containing the conjugated NPs. The absorbance values of these fractions were measured and summed to determine the total amount of conjugated dye. A standard curve was generated using various concentrations of AF-488 (Figure 7A), allowing for accurate determination of the dye concentration in the conjugated fractions. This approach is

consistent with previous studies that have used methods to quantify bioconjugation efficiency. [42]

The initial amount of DBCO added to the reaction was known from the synthesis protocol described in the previous section. Using this information, we calculated the percentage of reaction efficiency using the following equation:

$$Click\ Reaction\ efficiency(\%) = \frac{[Reactive\ DBCO]}{[Total\ DBCO]} \times 100$$

Equation 2: *The reaction efficiency is calculated as the concentration of reactive DBCO divided by the total DBCO added.*

Our analysis shows that with 0.25 µmol of DBCO on the surface of the NPs, the efficiency is around 10%. This efficiency decreases as the amount of DBCO is reduced (Figure 7B). We chose to stop at this level because the batch we used already had an average of 20% DBCO coverage on the surface. To increase efficiency beyond 10%, we would need to either combine batches with higher DBCO content or produce NPs that are at least double the normal batch. We also attempted to increase the dye proportions, but this approach failed to improve conjugation efficiency. This suggests that the limiting factor is not the dye concentration, but rather the availability of DBCO, possibly due to some DBCO molecules being internalized within the NPs and thus inaccessible for reaction. [69] Additionally, further increasing the DBCO may result in diminishing returns due to steric hindrance and could potentially compromise the stability and functionality of the NPs. [70] At this stage, we achieved 10% overall NPs conjugation efficiency, with 50% of the DBCO molecules on the surface successfully participating in the binding reaction. This indicates that while half of the available DBCO is active, there is still potential for further optimization to improve the overall NP-level efficiency.

In this study, we were able to calculate efficiency even with very low amounts of DBCO, whereas in a previous study [42] amounts below 0.5 mol% were insufficient for accurate calculation in nanoemulsion. Based on the literature, a 10% click efficiency can be considered adequate for certain applications, especially in fields like radiochemistry, where it has been shown to produce effective imaging agents. For example, in selective radiolabeling, even with just 10% efficiency, effective imaging compounds can still be produced. When this efficiency is combined with other techniques, the overall performance can be further improved. The simplicity and speed of click reactions make them valuable in research, allowing the production of diverse compounds, even at lower efficiencies.[71] [72] However, for other therapeutic applications, such as exosome modifications in cancer therapy, higher click efficiencies are often more desirable. Studies

have shown that improved click efficiencies lead to better targeting and delivery capabilities, which are crucial for overcoming cancer heterogeneity and enhancing treatment specificity.[73] In such cases, higher efficiency may be necessary to optimize therapeutic outcomes while maintaining NP stability and functionality. [74] Thus, while achieving higher click efficiencies is often critical in more demanding therapeutic contexts, lower efficiency may still be suitable for some applications.

A

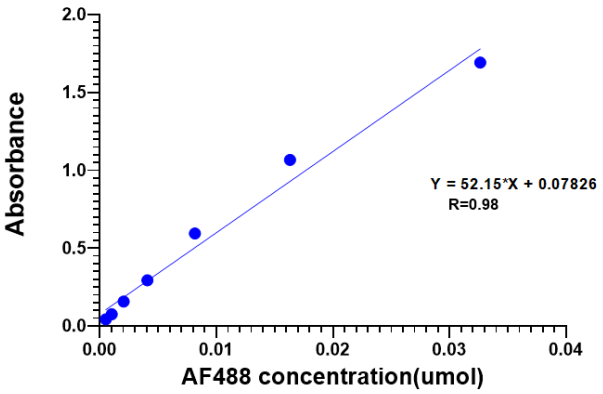

B

DBCO (umol)	bound DBCO (umol)	Click Reaction efficiency (%)
0.25	0.026	**10.5**
0.15	0.013	**8.7**
0.09	0.006	**6.5**
0.03	0.001	**3.4**

Figure 7: *A)a standard curve showing the relationship between AF488 concentration (µmol) and absorbance, used to quantify bound DBCO in the click reaction. B) Table summarizing DBCO concentration, bound DBCO, and click reaction efficiency at varying initial DBCO amounts.*

Following the successful optimization process with AF-488, the focus shifted to binding a model peptide to the NPs. For this purpose, the TAT-Lys(N_3)-6-FAM peptide was selected, featuring an N_3 terminal for reaction with DBCO and a 6-FAM dye for detection of the binding process. This strategy supports the broader objective of developing functionalized NPs designed for targeted cell interactions. By replacing a simple dye with a peptide that can target specific cell types, moving us closer to creating NPs suitable for targeted imaging or therapeutic applications.[75] Moreover, this is another approach where the azide-alkyne cycloaddition reaction is used to attach peptides to NPs, enhancing the stability and functionality of the conjugates. [15][76] [77]This redesign requires a new round of optimization, similar to the procedures defined in the previous section. The initial step involved determining the optimal molar ratio between DBCO and the peptide. Two ratios were examined: 2:1 and 1:1.In our previous optimization, we found that increasing the amount of DBCO while keeping the azide group constant did not provide enough azide groups to react with DBCO in a 3:1 ratio. To improve this, we adjusted the ratio to 2:1, then reduced it to 1:1 to evaluate the impact on reactivity.

Results indicated that the 2:1 ratio (2 mol DBCO and 1 mol peptide) again proved to be the most effective, while the 1:1 ratio resulted in an excess of unbound peptides (Figure

8A). Despite this observation, both molar ratios were maintained for further optimization to study whether factors like time and temperature could influence the amount of excess free peptide.

The presence of unbound peptides can reduce the efficiency of optimization steps and the bioactivity of NP-peptide conjugates. Free peptides may compete with bound peptides, lowering the yield and functionality of the final product. Additionally, they can interact with other molecules, reducing their availability for targeted pathways and compromising NP system effectiveness. [77] [78] Therefore, minimizing unbound peptides is crucial for optimizing performance and safety, and washing away excess peptides can enhance the overall quality of the conjugates.

Further optimization focuses on reaction time and temperature effects. When using a 1:1 molar ratio of DBCO to peptide, an increase in absorbance was observed in the bound fraction after 24 hours, accompanied by a decrease in free peptide (Figure 8B). Interestingly, no significant difference was found between reactions conducted at room temperature and 37°C (Figure 8C). This suggests that while extended time allows peptides better access to surface DBCO groups, temperature does not play a key role in this process. In contrast, when employing a 2:1 molar ratio of DBCO to peptide, neither reaction time nor temperature significantly influenced the conjugation efficiency (Figures 8D-E). This indicates that the 2:1 ratio provides an optimal proportion of DBCO and peptide for efficient binding, regardless of these parameters. These findings suggest that where the amount of DBCO on the NPs surface is limited, using a 1:1 molar ratio with an extended reaction time of 24 hours can effectively develop peptide access to the available DBCO groups.

The optimization of reaction time and temperature in peptide-NP binding using DBCO and azide chemistry highlights several findings. The increase in absorbance observed with a 1:1 molar ratio after 24 hours suggests that extended reaction time enhances peptide access to DBCO groups, likely due to increased interaction opportunities.[79] Importantly, the lack of a significant temperature effect between room temperature and 37°C indicates that the reaction is not highly temperature-dependent, which is beneficial for practical applications where precise temperature control may be challenging.[65] In contrast, in the 2:1 molar ratio, the efficiency appears to be optimal regardless of time or temperature, suggesting that the excess DBCO provides sufficient reactive sites for peptide binding, making these parameters less critical.[80]

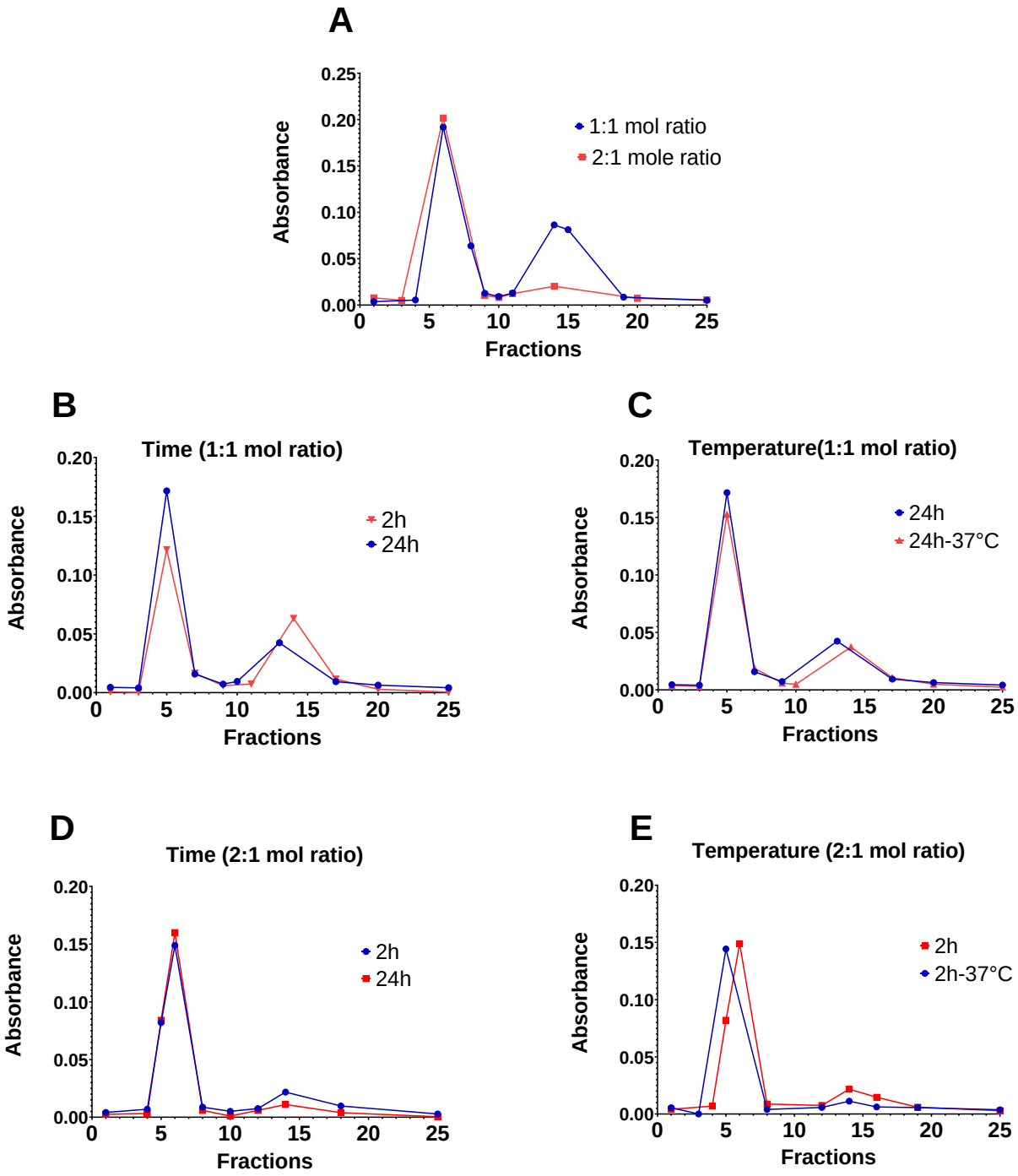

Figure 8: *A) Absorbance of fractions collected during the separation process for 1:1 (blue) and 2:1 (red) DBCO-to-peptide mole ratios. B) Effect of reaction time (2 hours vs. 24 hours at room temperature) on absorbance for 1:1 mole ratio. C) Effect of temperature (24 hours at room temperature vs. 24 hours at 37°C) on absorbance for 1:1 mole ratio. D) Effect of temperature (2 hours at room temperature vs. 2 hours at 37°C) on absorbance for 2:1 mole ratio. E) Effect of reaction time (2 hours vs. 24 hours at room temperature) on absorbance for 2:1 mole ratio.*

Click Reaction Characterization

Following the comprehensive optimization process, the occurrence of the click reaction was confirmed through Fourier-transform infrared (FT-IR) Spectroscopy and ^{1}H NMR analyses. The FT-IR analysis yielded particularly insightful results, providing clear spectral evidence of the newly formed chemical bonds and functional groups characteristic of the click reaction products. This spectroscopic data is complemented by the ^{1}H NMR findings. Before the DBCO-TAT conjugation, we observed a distinct peak (red) in the 2100-2160 cm^{-1} range of the peptide-containing sample's spectrum (Figure 9). This peak corresponds to the azide ($-N_3$) group stretching vibration, which is characteristic of the TAT-Lys(N_3)-6-FAM peptide. The presence of this peak clearly indicates unreacted peptides.

After the click reaction between the DBCO-functionalized NPs and the azide-modified peptide (blue), the FT-IR spectrum showed a significant reduction, or in some cases, complete disappearance, of the azide peak. This observation confirms that the majority of azide groups were consumed in the cycloaddition reaction with the DBCO groups present on the NPs surface, similar to results found in previous studies involving azide-functionalized peptides and NPs.[81][82] The absence of the azide peak in the spectrum after the reaction indicates that the majority of the azide groups have been consumed in the cycloaddition reaction with the DBCO on the NP surface. This result suggests a high degree of conjugation efficiency, which is a key advantage of the SPAAC reaction in bioconjugation applications.[83]

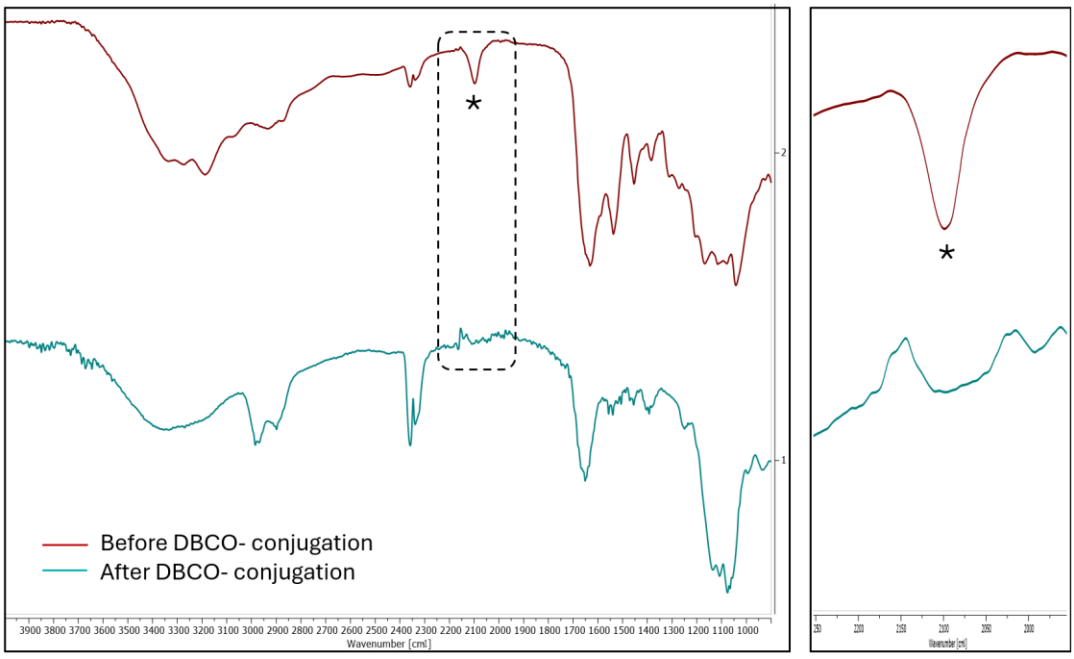

Figure 9: *FTIR spectra comparing samples before and after DBCO conjugation with TAT peptide.*

To further confirm the structural changes at the molecular level, ^{1}H NMR was employed. The NMR analysis revealed changes in the chemical environment of protons, indicating the formation of the triazole linkage between the azide and alkyne groups. [84] The ^{1}HNMR analysis of the PEGylated NPs before and after the click reaction with the peptide reveals several key observations. The PLGA peaks at 1.5, 4.8, and 5.2 ppm remain unchanged, indicating the stability of the PLGA structure throughout the process (Figure 10). Notably, the complete disappearance of PVA surfactant signals after two washing steps confirms the effective purification of the NPs. In contrast, there is an increase in intensity in the aromatic region (6.5-8.5 ppm) following the click reaction, related to the aromatic structures in the 6-FAM (fluorescein) of the attached peptide. Importantly, a new signal around 8.45 ppm appears, characteristic of the triazole proton formed during the click reaction, serving as a key indicator of successful conjugation.[85] However, the relatively low intensity of this peak is consistent with the expected outcome, given that the click reaction involves only 10% of the total NPs. This lower signal intensity, compared to the higher peaks associated with PLGA (1.5,4.8, and 5.2 ppm)[52] , is due to the many repeating monomer units in the polymer, which generate a stronger signal. These findings highlight the successful binding of the peptide to the NPs and the detection of surface modifications using ^{1}H NMR spectroscopy.

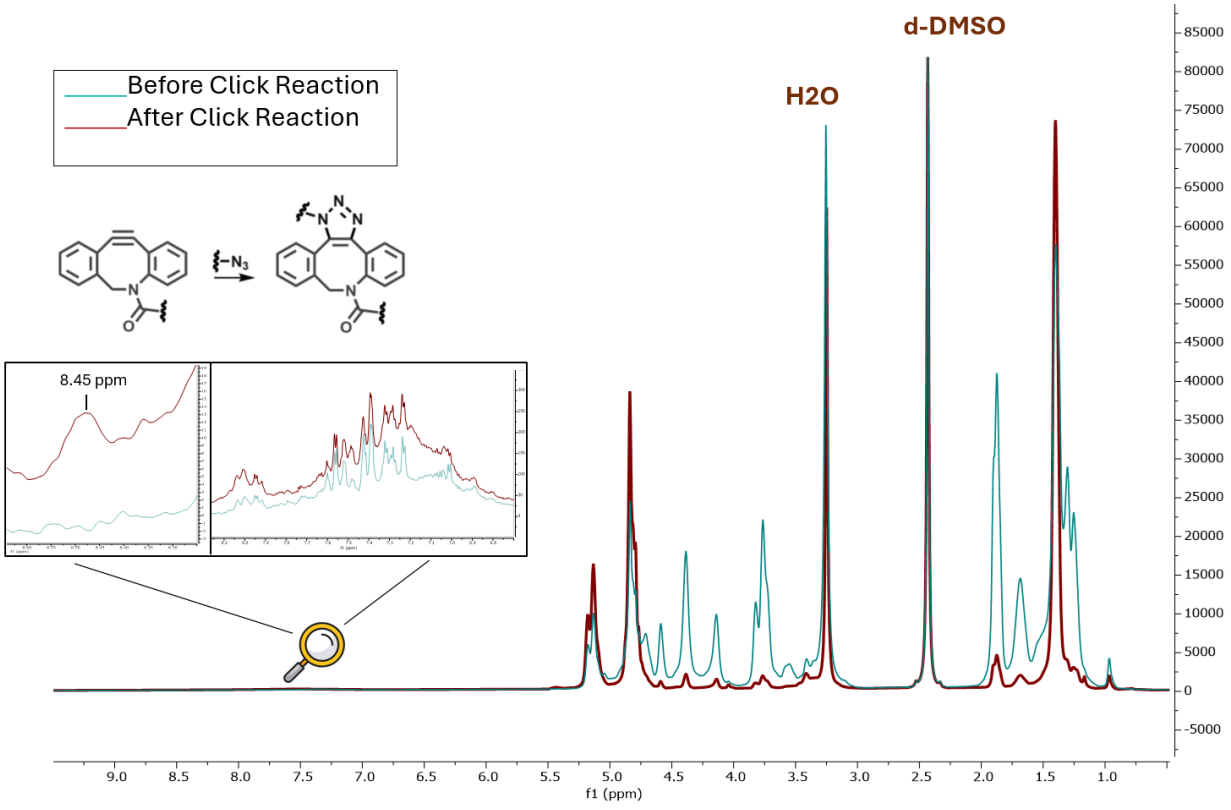

Figure 10 : *Comparison of ^{1}H NMR Spectra Before and After Click Reaction*

Cellular Uptake, Confocal Microscopy and Viability Assessment

In this study, we used HeLa-80 cells to evaluate the cellular uptake and biocompatibility of NPs functionalized with AF488 and TAT peptide. HeLa-80 cells are a commonly used model in cancer research due to their rapid growth and responsiveness, which makes them ideal for studying drug delivery and NP uptake. [86] These cells closely mimic tumor cell behavior, offering a relevant platform for investigating the efficiency of NP-based therapies.[87] Their well-characterized structure further enhances the reliability of results, especially in experiments involving functionalized NPs.[88]

The TAT peptide was chosen for NP functionalization because of its recognized ability to enhance cellular uptake in some cells. This cell-penetrating peptide (CPP) is known for facilitating the intracellular delivery of molecules through receptor-mediated endocytosis, making it particularly useful for enhancing the internalization of NPs in cancer cells.[89][90][91]This experiment aimed to compare the internalization efficiency of TAT-functionalized NPs (PNP+TAT) with that of dye-labeled NPs (PNP+Dye) over time and to determine whether TAT could enhance cellular uptake compared to NPs without it.

To achieve this, flow cytometry was employed to monitor NP uptake by HeLa-80 cells at various time points. Initially, we observed no significant uptake of either PNP+Dye or PNP+TAT at 3 and 5 hours, as shown in Figure 11A. However, by 20 hours, a noticeable increase in NP internalization occurred in the PNP+Dye, while the PNP+TAT showed limited uptake (Figure 11A).

In subsequent experiments, we adjusted the time points to focus on longer intervals (6, 14, 18, and 24 hours) and included Attoxa-loaded NPs (NP-Attoxa) as a control. Flow cytometry analysis was employed to evaluate NP uptake across different conditions. The gating strategy was as follows: First, forward scatter (FSC) and side scatter (SSC) were used to select the cell population. Next, we applied an FSC-A vs. FSC-H plot to discriminate singlets. The live cell population was gated using UV405 (detected via Zombie UV). Finally, NP-positive populations were identified using the appropriate fluorescence channels for each sample (via histograms corresponding to the specific dye associated with each NP formulation).

Flow cytometry analysis revealed that in positive populations both NP-Attoxa and PNP+Dye exhibited nearly 100% uptake by 6 hours, contrary to expectations, as we had anticipated higher uptake in the PNP+TAT group due to the cell-penetrating properties of the TAT peptide (Figure 11B). Surprisingly, PNP+TAT displayed almost no uptake at 6 hours, and by 24 hours, uptake remained below 50%. In contrast, PNP+Dye and NP-Attoxa consistently showed close to 100% uptake throughout the experiment. The unexpected results observed with PNP+TAT showing lower uptake compared to PNP+Dye and NP-Attoxa can be attributed to several factors. Firstly, adding the TAT peptide may have altered the NPs' surface properties, potentially changing their overall

charge, reducing interaction with cell membranes, and diminishing their effective concentration for cellular uptake.[92] Secondly, the presence of TAT could trigger different cellular responses, such as alternative endocytic pathways that are less efficient or rapid exocytosis of internalized particles. [93] Lastly, technical considerations may play a role, including potential fluorescence quenching by the TAT peptide which might be higher than dye, strong membrane association of PNP+Dye particles after washing giving a false impression of high uptake, or limitations in the sensitivity of flow cytometry for detecting low levels of PNP+TAT uptake. [94]

When analyzing the raw, baseline-corrected data, we observed a rapid increase in PNP+Dye uptake between 6 and 14 hours. After 14 hours, the uptake plateaued, indicating that most of the dye-labeled NPs were uptaken by the cells early in the experiment. Beyond this point, there was no significant difference between the 14- and 18-hour time points, with only a slight increase at 24 hours(Figure 11C). In contrast, NP-Attoxa showed a stable uptake pattern throughout the entire experiment, while PNP+TAT exhibited a slow but steady increase in uptake over time.

Notably, when we normalized the data to the first time point, PNP+TAT exhibited a more significant increase in uptake over time compared to PNP+Dye and NP-Attoxa (Figure 11D). This delayed uptake can be attributed to time-dependent phenomena, reflecting a slower interaction of TAT-functionalized NPs with the cells. PNP+TAT may require longer incubation times for significant internalization, possibly due to their unique surface properties or alternative uptake mechanisms. [95] In contrast, PNP+Dye and NP-Attoxa both reached near saturation quickly, with PNP+Dye exhibiting near 100% uptake early on, as shown in Figure 11B. This rapid uptake leads to a plateau, likely caused by the saturation of available binding sites on the cell surface or intracellular processing pathways becoming fully engaged.[96] [97] [94]

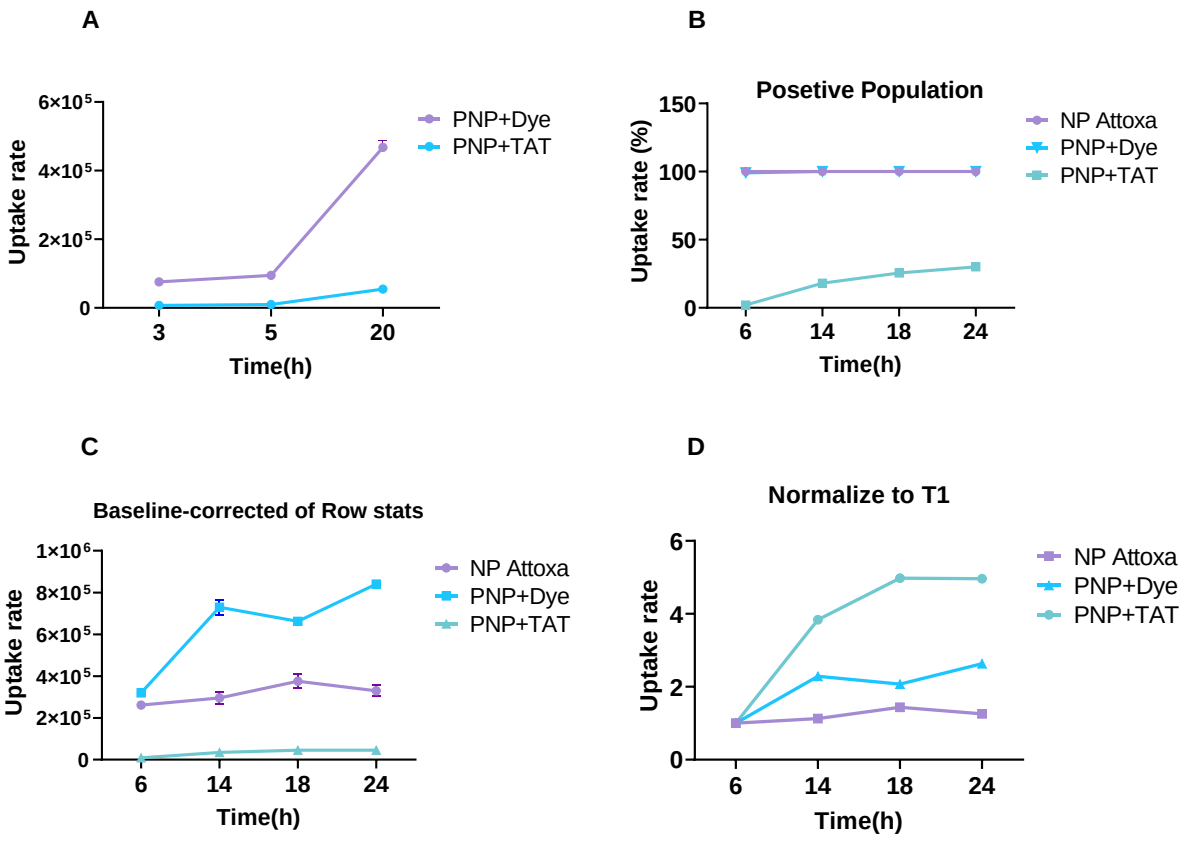

Figure 11 : *Cellular uptake of NPs over time. A) Schematic representation of NP formulations: PNP+Dye, and PNP+TAT. B) Percentage of positive cells (cells that have taken up nanoparticles) at 6, 14, 18, and 24 hours. C) Raw, baseline-corrected fluorescence intensity data showing NP uptake over time. D) Normalized uptake data relative to the first time point (6 hours).*

Confocal imaging was used primarily to verify the presence of NPs inside the cells, providing visual confirmation of their internalization. The objective was to assess whether the NPs, specifically PNP+Dye, and PNP+TAT, could be detected interacting with the cells despite the lower efficiency of the click reaction (~10%). We aimed to ensure that, even with lower uptake levels, the NPs were still visible inside HeLa-80 cells, which are known to uptake less than Phagocytic cells.[98]

At the 6-hour time point, confocal imaging showed no interaction between the cells and either PNP+Dye or PNP+TAT (Figure 12). This was surprising, as flow cytometry had indicated nearly 100% uptake of PNP+Dye at the same time point. By 24 hours, however, confocal imaging confirmed a significant accumulation of PNP+Dye within the cells, which aligned with the flow cytometry results at that later stage.

The discrepancies observed between flow cytometry and confocal microscopy results, particularly at early time points like 6 hours, can be explained by the characteristics and limitations of each technique in analyzing NP uptake.

Flow cytometry, as a highly sensitive technique, detects even small amounts of fluorescence and measures the total fluorescence from a large population of cells. However, this sensitivity often leads to an overestimation of NP uptake. The method cannot differentiate between NPs attached to the cell membrane and those internalized, potentially resulting in false positives. [98] This issue is particularly problematic with NPs like NP-Attoxa, which may release the dye. The released dye can associate with cell membranes, producing a signal that reflects attachment rather than true internalization. This phenomenon emphasizes the importance of employing multiple complementary techniques to verify and characterize NPs uptake accurately. [99] Conversely, confocal microscopy provides spatially detailed images, enabling more precise localization of NPs inside or outside cells. [100] However, it is less sensitive to low fluorescence levels compared to flow cytometry. At early time points like 6 hours, or when working with small quantities of NPs, the fluorescence might be too weak for detection, especially near the sensitivity limits of the instrument. [101] [102] Moreover, confocal microscopy faces physical challenges, including laser power, photobleaching, and signal-to-noise ratio, which can impact image quality. Several factors, such as detector sensitivity, image acquisition settings, and the sample's optical properties, also influence the accuracy and reliability of imaging. These issues make detecting weak signals more difficult, particularly when analyzing small quantities of NPs at early stages. [103]

Overall, flow cytometry indicated a high uptake of PNP+Dye at the 6-hour time point; however, this was not confirmed by confocal microscopy. This suggests that the flow cytometry data may reflect particle attachment to the membrane rather than true internalization. Additionally, the lower sensitivity of confocal microscopy may have failed to detect weak fluorescence from internalized particles. These findings suggest that further repetition of both confocal and flow cytometry experiments is necessary to clarify the exact nature of NP uptake and ensure the accuracy of the results.

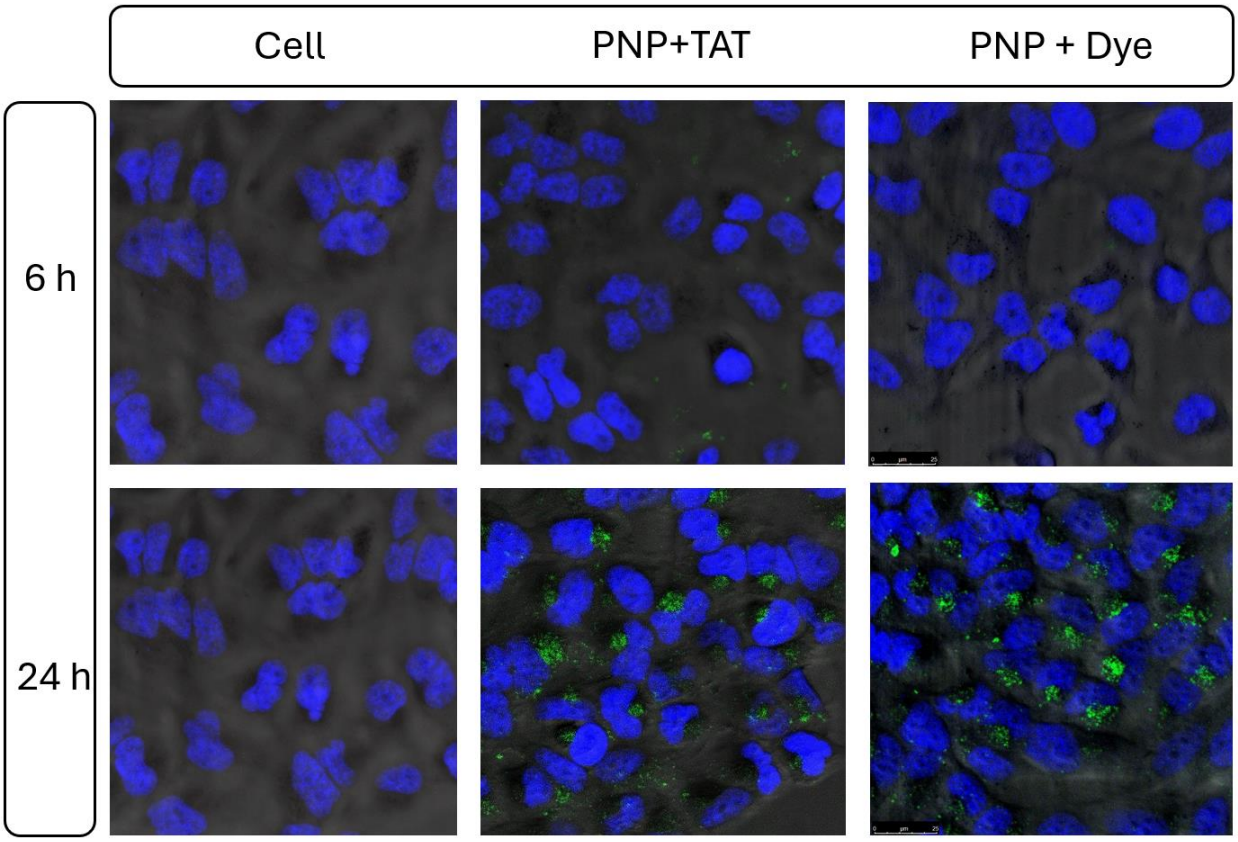

Figure 12: *Confocal microscopy images at 6 and 24 hours for PNP+Dye and PNP+TAT*

In addition to uptake and confocal imaging, we evaluated the biocompatibility of the NPs by measuring cell viability using flow cytometry. To measure cell viability in this experiment, flow cytometry was used with Zombie UV, a viability dye chosen to minimize background interference from the fluorescent labels used on the NPs. This approach helped reduce the overlap between the fluorescence signals of the NPs and the viability dye, ensuring more accurate viability assessments.

The cell viability results from Figure 13A-B demonstrate that all three types of NPs—PNP+Dye, PNP+TAT, and NP-Attoxa—are generally biocompatible with HeLa-80 cells, maintaining high viability even after 24 hours of exposure. The control group consistently showed 100% viability, confirming that the experimental conditions did not affect the cells. Both PNP+Dye and PNP+TAT follow a similar pattern over time, with high cell viability throughout. However, the main difference is at the beginning: PNP+Dye starts with slightly lower viability compared to PNP+TAT but gradually increases, eventually reaching levels close to PNP+TAT at later time points. NP-Attoxa shows a gradual decline in viability, dropping to around 90% by 24 hours, indicating a modest effect. This pattern of viability

is consistent with the typical behavior of our NPs.[104] Although there is no specific literature confirming the viability of these particular NPs in HeLa-80 cells, studies have shown that PLGA NPs exhibit good biocompatibility, maintaining high cell viability with minimal cytotoxic effects across various cell types and formulations. [105][106][107]

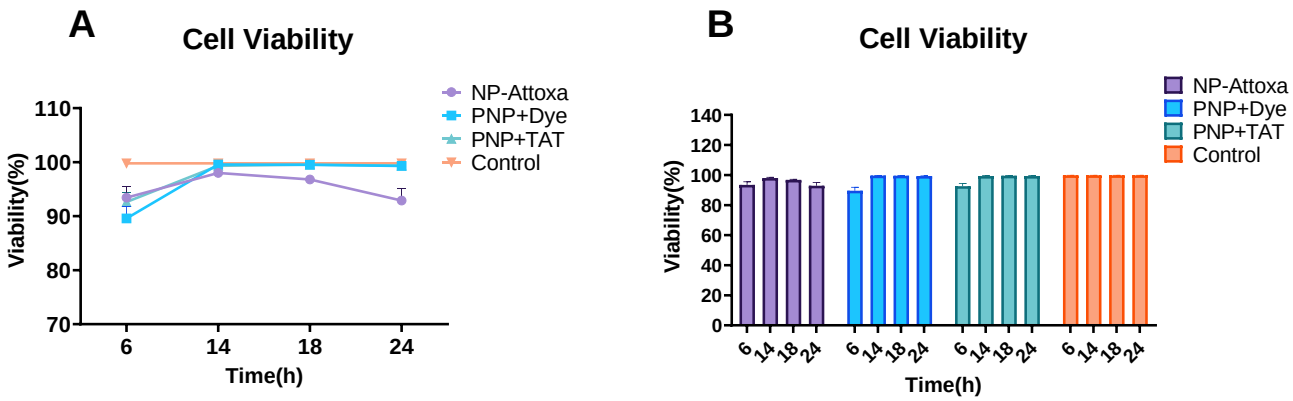

Figure 13: *Cell viability assessment of NPs in HeLa-80 cells. A) xy graph showing cell viability over time (6, 14, 18, and 24 hours) for PNP+Dye, PNP+TAT, and NP-Attoxa compared to control. B) Bar graph representation of cell viability at 24 hours for each NP type.*

4 Conclusion

In conclusion, this study successfully optimized the click chemistry conditions for functionalizing NPs with both Dye and peptides, focusing on parameters such as the DBCO-to-azide tagged molecule ratio, reaction time, and temperature. We found that a 2:1 ratio of DBCO to AF-488 dye produced the highest conjugation efficiency, likely due to reduced steric hindrance, which improved accessibility to DBCO sites on the NP surface. The optimal ratio was confirmed by SEC, which showed higher absorbance in the conjugated fractions and a decrease in unreacted dye. Notably, extending reaction time beyond 2 hours or increasing temperature had minimal impact on the efficiency of the conjugation, suggesting that the reaction proceeds to completion effectively under mild conditions.

The same 2:1 ratio was also effective for conjugating TAT-Lys(N3)-6-FAM peptide to NPs, with longer reaction times enhancing peptide conjugation, particularly when DBCO availability was limited. FT-IR and ^{1}H NMR analyses further validated the success of the click reaction, confirming both the reduction of azide groups and the formation of triazole linkages, key indicators of successful conjugation.

Additionally, the optimization of NPs with TAT and dye in this study led to the development of a highly effective NP formulation for in vitro testing. Flow cytometry demonstrated significant uptake of PNP+Dye by HeLa-80 cells. PNP+Dye exhibited rapid saturation, while PNP+TAT showed a slower, steady increase in uptake over time, likely due to the TAT peptide altering the internalization process. Despite the low click reaction efficiency of approximately 10%, confocal microscopy successfully confirmed the internalization of NPs, demonstrating the formulation's effectiveness and resilience within cellular environments. However, there is potential to further improve the click reaction efficiency. Strategies such as optimizing PEGylation to increase DBCO surface density or increasing the concentration of PNP to react more effectively with azide-tagged molecules.

Viability testing showed promising results, with cell viability exceeding 90% after 24 hours of exposure to the NPs. Although NP-Attoxa caused a slight reduction in viability, both PNP+Dye and PNP+TAT maintained consistently high viability levels, indicating that the NPs are safe and minimally cytotoxic in cellular models.

In summary, this study has successfully developed and optimized NPs that achieve both high cellular uptake and excellent biocompatibility, establishing a strong foundation for their potential use in target imaging and therapeutic applications. These findings pave the way for future research to explore the performance of these NPs in more complex biological systems and their potential for targeted delivery in disease models. Future research should focus on replicating these in vitro tests with various cell-penetrating peptides and across different cell lines to gain a broader understanding of NP efficacy.

5 Acknowledgements

I gratefully acknowledge Naiara Larreina Vicente (CBI department, Wageningen University and Research) for providing TAT peptide, HeLa-80 cells, and assistance with in vitro experiments and confocal microscopy. Thanks to the Department of Physical Chemistry and Soft Matter for access to dynamic light scattering equipment, and the Department of Organic Chemistry for the use of their FT-IR and NMR spectrometers. Their support was invaluable to this research.

[1] Y. D. Xiao, R. Paudel, J. Liu, C. Ma, Z. S. Zhang, and S. K. Zhou, “MRI contrast agents: Classification and application (Review),” Nov. 01, 2016, *Spandidos Publications*. doi: 10.3892/ijmm.2016.2744.

[2] I. Tirotta *et al.*, “19F magnetic resonance imaging (MRI): From design of materials to clinical applications,” Jan. 28, 2015, *American Chemical Society*. doi: 10.1021/cr500286d.

[3] A. Mali, E. L. Kaijzel, H. J. Lamb, and L. J. Cruz, “19F-nanoparticles: Platform for in vivo delivery of fluorinated biomaterials for 19F-MRI,” *Journal of Controlled Release*, vol. 338, pp. 870–889, Oct. 2021, doi: 10.1016/j.jconrel.2021.09.001.

[4] C. Grapentin, S. Barnert, and R. Schubert, “Monitoring the stability of perfluorocarbon nanoemulsions by Cryo-TEM image analysis and dynamic light scattering,” *PLoS One*, vol. 10, no. 6, Jun. 2015, doi: 10.1371/journal.pone.0130674.

[5] L. Wu, F. Liu, S. Liu, X. Xu, Z. Liu, and X. Sun, “Perfluorocarbons-based19f magnetic resonance imaging in biomedicine,” 2020, *Dove Medical Press Ltd*. doi: 10.2147/IJN.S255084.

[6] H. Sah, L. A. Thoma, H. R. Desu, E. Sah, and G. C. Wood, “Concepts and practices used to develop functional PLGA-based nanoparticulate systems,” Feb. 21, 2013. doi: 10.2147/IJN.S40579.

[7] O. Koshkina *et al.*, “Multicore Liquid Perfluorocarbon-Loaded Multimodal Nanoparticles for Stable Ultrasound and 19 F MRI Applied to In Vivo Cell Tracking,” *Adv Funct Mater*, vol. 29, no. 19, May 2019, doi: 10.1002/adfm.201806485.

[8] A. H. J. Staal *et al.*, “In vivo clearance of 19F MRI imaging nanocarriers is strongly influenced by nanoparticle ultrastructure,” *Biomaterials*, vol. 261, Dec. 2020, doi: 10.1016/j.biomaterials.2020.120307.

[9] E. Swider *et al.*, “Design of triphasic poly(lactic-co-glycolic acid) nanoparticles containing a perfluorocarbon phase for biomedical applications,” *RSC Adv*, vol. 8, no. 12, pp. 6460–6470, 2018, doi: 10.1039/c7ra13062g.

[10] B. P. Joshi and T. D. Wang, “Targeted Optical Imaging Agents in Cancer: Focus on Clinical Applications,” 2018, *Hindawi Limited*. doi: 10.1155/2018/2015237.

[11] M. Azizi *et al.*, “Interactions Between Tumor Biology and Targeted Nanoplatforms for Imaging Applications,” May 01, 2020, *Wiley-VCH Verlag*. doi: 10.1002/adfm.201910402.

[12] M. M. Kaneda, S. Caruthers, G. M. Lanza, and S. A. Wickline, “Perfluorocarbon Nanoemulsions for quantitative molecular imaging and targeted therapeutics,” *Ann Biomed Eng*, vol. 37, no. 10, pp. 1922–1933, Oct. 2009, doi: 10.1007/s10439-009-9643-z.

[13] G. Zambito *et al.*, “Fluorinated PLGA-PEG-Mannose Nanoparticles for Tumor-Associated Macrophage Detection by Optical Imaging and MRI,” *Front Med (Lausanne)*, vol. 8, Aug. 2021, doi: 10.3389/fmed.2021.712367.

[14] E. Hoogendijk *et al.*, “Continuous-Flow Production of Perfluorocarbon-Loaded Polymeric Nanoparticles: From the Bench to Clinic,” *ACS Appl Mater Interfaces*, vol. 12, no. 44, pp. 49335–49345, Nov. 2020, doi: 10.1021/acsami.0c12020.

[15] P. M. Winter, K. Cai, S. D. Caruthers, S. A. Wickline, and G. M. Lanza, “Emerging nanomedicine opportunities with perfluorocarbon nanoparticles,” Mar. 2007. doi: 10.1586/17434440.4.2.137.

[16] H. K. Makadia and S. J. Siegel, “Poly Lactic-co-Glycolic Acid (PLGA) as biodegradable controlled drug delivery carrier,” *Polymers (Basel)*, vol. 3, no. 3, pp. 1377–1397, Sep. 2011, doi: 10.3390/polym3031377.

[17] X. Li *et al.*, “Recent advances in targeted nanoparticle drug delivery systems for ischaemic stroke,” Sep. 30, 2023, *Royal Society of Chemistry*. doi: 10.1039/d3ma00472d.

[18] Y. Zhong, F. Meng, C. Deng, and Z. Zhong, “Ligand-directed active tumor-targeting polymeric nanoparticles for cancer chemotherapy,” Jun. 09, 2014, *American Chemical Society*. doi: 10.1021/bm5003009.

[19] Y. Yan *et al.*, “Sequential Modulations of Tumor Vasculature and Stromal Barriers Augment the Active Targeting Efficacy of Antibody-Modified Nanophotosensitizer in Desmoplastic Ovarian Carcinoma,” *Advanced Science*, vol. 8, no. 3, Feb. 2021, doi: 10.1002/advs.202002253.

[20] K. Hemant, P. S. Shashi, K. Jitender, K. Pramod, and P. Balaram, “December (2022) Res.”

[21] N. Alsawaftah, W. G. Pitt, and G. A. Husseini, “Dual-Targeting and Stimuli-Triggered Liposomal Drug Delivery in Cancer Treatment,” Jun. 11, 2021, *American Chemical Society*. doi: 10.1021/acsptsci.1c00066.

[22] K. Hemant, P. S. Shashi, K. Jitender, K. Pramod, and P. Balaram, “December (2022) Res.”

[23] C. Comanescu, “Recent Advances in Surface Functionalization of Magnetic Nanoparticles,” Oct. 01, 2023, *Multidisciplinary Digital Publishing Institute (MDPI)*. doi: 10.3390/coatings13101772.

[24] J. Yoo, K. Kim, S. Kim, H. H. Park, H. Shin, and J. Joo, “Tailored polyethylene glycol grafting on porous nanoparticles for enhanced targeting and intracellular siRNA delivery,” *Nanoscale*, vol. 14, no. 39, pp. 14482–14490, Sep. 2022, doi: 10.1039/d2nr02995b.

[25] D. Zhang *et al.*, “Drug-loaded PEG-PLGA nanoparticles for cancer treatment,” Aug. 19, 2022, *Frontiers Media S.A.* doi: 10.3389/fphar.2022.990505.

[26] L. Shi *et al.*, “Effects of polyethylene glycol on the surface of nanoparticles for targeted drug delivery,” Jun. 28, 2021, *Royal Society of Chemistry*. doi: 10.1039/d1nr02065j.

[27] D. L. J. Thorek, D. R. Elias, and A. Tsourkas, “Comparative analysis of nanoparticle-antibody conjugations: Carbodiimide versus click chemistry,” *Mol Imaging*, vol. 8, no. 4, pp. 221–229, Jul. 2009, doi: 10.2310/7290.2009.00021.

[28] T. N. Gevrek, I. Kosif, and A. Sanyal, “Surface-Anchored Thiol-Reactive Soft Interfaces: Engineering Effective Platforms for Biomolecular Immobilization and Sensing,” *ACS Appl Mater Interfaces*, vol. 9, no. 33, pp. 27946–27954, Aug. 2017, doi: 10.1021/acsami.7b07779.

[29] M. Abe, P. Akbarzaderaleh, M. Hamachi, N. Yoshimoto, and S. Yamamoto, “Interaction mechanism of mono-PEGylated proteins in electrostatic interaction chromatography,” *Biotechnol J*, vol. 5, no. 5, pp. 477–483, May 2010, doi: 10.1002/biot.201000013.

[30] S. Lee *et al.*, “Chemical tumor-targeting of nanoparticles based on metabolic glycoengineering and click chemistry,” *ACS Nano*, vol. 8, no. 3, pp. 2048–2063, Mar. 2014, doi: 10.1021/nn406584y.

[31] G. Von Maltzahn *et al.*, “In vivo tumor cell targeting with ‘click’ nanoparticles,” *Bioconjug Chem*, vol. 19, no. 8, pp. 1570–1578, 2008, doi: 10.1021/bc800077y.

[32] H. Struthers, T. L. Mindt, and R. Schibli, “Metal chelating systems synthesized using the copper(I) catalyzed azide-alkyne cycloaddition,” *Dalton Transactions*, vol. 39, no. 3, pp. 675–696, 2010, doi: 10.1039/b912608b.

[33] B. T. Worrell, J. A. Malik, and V. V. Fokin, “Direct evidence of a dinuclear copper intermediate in Cu(I)-catalyzed azide-alkyne cycloadditions,” *Science (1979)*, vol. 340, no. 6131, pp. 457–460, Apr. 2013, doi: 10.1126/science.1229506.

[34] P. K. Mishra, N. Sharma, H. Kim, C. Lee, and H. W. Rhee, “GEN-Click: Genetically Encodable Click Reactions for Spatially Restricted Metabolite Labeling,” *ACS Cent Sci*, vol. 9, no. 8, pp. 1650–1657, Aug. 2023, doi: 10.1021/acscentsci.3c00511.

[35] D. Bauer, M. A. Cornejo, T. T. Hoang, J. S. Lewis, and B. M. Zeglis, “Click Chemistry and Radiochemistry: An Update,” Nov. 15, 2023, *American Chemical Society*. doi: 10.1021/acs.bioconjchem.3c00286.

[36] S. S. Vanberkel *et al.*, “Traceless tosylhydrazone-based triazole formation: A metal-free alternative to strain-promoted azide-alkyne cycloaddition,” *Angewandte Chemie - International Edition*, vol. 51, no. 22, pp. 5343–5346, May 2012, doi: 10.1002/anie.201108850.

[37] I. Krizhanovskiy, M. Temnikov, Y. Kononevich, A. Anisimov, F. Drozdov, and A. Muzafarov, “The Use of the Thiol-Ene Addition Click Reaction in the Chemistry of Organosilicon Compounds: An Alternative or a Supplement to the Classical Hydrosilylation?,” Aug. 01, 2022, *MDPI*. doi: 10.3390/polym14153079.

[38] J. P. Meyer, P. Adumeau, J. S. Lewis, and B. M. Zeglis, “Click Chemistry and Radiochemistry: The First 10 Years,” Dec. 21, 2016, *American Chemical Society*. doi: 10.1021/acs.bioconjchem.6b00561.

[39] V. Bouvet, M. Wuest, and F. Wuest, “Copper-free click chemistry with the short-lived positron emitter fluorine-18,” *Org Biomol Chem*, vol. 9, no. 21, pp. 7393–7399, Nov. 2011, doi: 10.1039/c1ob06034a.

[40] S. Arumugam, J. Chin, R. Schirrmacher, V. V. Popik, and A. P. Kostikov, “[18F]Azadibenzocyclooctyne ([18F]ADIBO): A biocompatible radioactive labeling synthon for peptides using catalyst free [3+2] cycloaddition,” *Bioorg Med Chem Lett*, vol. 21, no. 23, pp. 6987–6991, Dec. 2011, doi: 10.1016/j.bmcl.2011.09.126.

[41] J. M. Baskin *et al.*, “Copper-free click chemistry for dynamic in vivo imaging,” 2007. [Online]. Available: www.pnas.org/cgi/content/full/

[42] A. S. Perez *et al.*, “Click-Ready Perfluorocarbon Nanoemulsion for 19F MRI and Multimodal Cellular Detection,” *ACS Nanoscience Au*, vol. 2, no. 2, pp. 102–110, Apr. 2022, doi: 10.1021/acsnanoscienceau.1c00016.

[43] J. Dommerholt, F. P. J. T. Rutjes, and F. L. van Delft, “Strain-Promoted 1,3-Dipolar Cycloaddition of Cycloalkynes and Organic Azides,” Apr. 01, 2016, *Springer International Publishing*. doi: 10.1007/s41061-016-0016-4.

[44] G. W. Liu, J. W. Pippin, D. G. Eng, S. Lv, S. J. Shankland, and S. H. Pun, “Nanoparticles exhibit greater accumulation in kidney glomeruli during experimental glomerular kidney disease,” *Physiol Rep*, vol. 8, no. 15, Aug. 2020, doi: 10.14814/phy2.14545.

[45] M. Alshamrani, “Broad-Spectrum Theranostics and Biomedical Application of Functionalized Nanomaterials,” Mar. 01, 2022, *MDPI*. doi: 10.3390/polym14061221.

[46] O. Veiseh, J. W. Gunn, and M. Zhang, “Design and fabrication of magnetic nanoparticles for targeted drug delivery and imaging,” Mar. 08, 2010. doi: 10.1016/j.addr.2009.11.002.

[47] Z. Fu and J. Xiang, “Aptamer-functionalized nanoparticles in targeted delivery and cancer therapy,” Dec. 01, 2020, *MDPI AG*. doi: 10.3390/ijms21239123.

[48] K. Ma and U. Wiesner, “Modular and Orthogonal Post-PEGylation Surface Modifications by Insertion Enabling Penta-Functional Ultrasmall Organic-Silica Hybrid Nanoparticles,” *Chemistry of Materials*, vol. 29, no. 16, pp. 6840–6855, Aug. 2017, doi: 10.1021/acs.chemmater.7b02009.

[49] L. Baghirova, E. K. Tilki, and A. A. Öztürk, “Evaluation of Cell Proliferation and Wound Healing Effects of Vitamin A Palmitate-Loaded PLGA/Chitosan-Coated PLGA Nanoparticles: Preparation, Characterization, Release, and Release Kinetics,” *ACS Omega*, vol. 8, no. 2, pp. 2658–2668, Jan. 2023, doi: 10.1021/acsomega.2c07232.

[50] B. Lu, X. Lv, and Y. Le, “Chitosan-modified PLGA nanoparticles for control-released drug delivery,” *Polymers (Basel)*, vol. 11, no. 2, Feb. 2019, doi: 10.3390/polym11020304.

[51] E. Swider *et al.*, “Förster Resonance Energy Transfer-Based Stability Assessment of PLGA Nanoparticles in Vitro and in Vivo,” *ACS Appl Bio Mater*, vol. 2, no. 3, pp. 1131–1140, Mar. 2019, doi: 10.1021/acsabm.8b00754.

[52] Q. Zhang, N. Guo, Y. Sun, X. Li, and H. Yang, “Absolute quantification of poly(DL-lactide-co-glycolide) in microspheres using quantitative 1H NMR spectroscopy,” *J Pharm Biomed Anal*, vol. 146, pp. 273–278, Nov. 2017, doi: 10.1016/j.jpba.2017.08.046.

[53] I. Korbag and S. Mohamed Saleh, “Studies on the formation of intermolecular interactions and structural characterization of polyvinyl alcohol/lignin film,” *International Journal of Environmental Studies*, vol. 73, no. 2, pp. 226–235, Mar. 2016, doi: 10.1080/00207233.2016.1143700.

[54] V. C. Pierre, J. L. Pasek-Allen, R. K. Wilharm, and J. C. Bischof, “NMR Characterization of Polyethylene Glycol Conjugates for Nanoparticle Functionalization,” *ACS Omega*, vol. 8, no. 4, pp. 4331–4336, Jan. 2023, doi: 10.1021/ACSOMEGA.2C07669.

[55] K. Barker *et al.*, “Biodegradable DNA-enabled poly(ethylene glycol) hydrogels prepared by copper-free click chemistry,” *J Biomater Sci Polym Ed*, vol. 27, no. 1, pp. 22–39, Jan. 2016, doi: 10.1080/09205063.2015.1103590.

[56] G. Yi, J. Son, J. Yoo, C. Park, and H. Koo, “Application of click chemistry in nanoparticle modification and its targeted delivery,” Apr. 13, 2018, *BioMed Central Ltd*. doi: 10.1186/s40824-018-0123-0.

[57] J. A. Finbloom, K. Han, C. C. Slack, A. L. Furst, and M. B. Francis, “Cucurbit[6]uril-Promoted Click Chemistry for Protein Modification,” *J Am Chem Soc*, vol. 139, no. 28, pp. 9691–9697, Jul. 2017, doi: 10.1021/jacs.7b05164.

[58] F. Alonso, Y. Moglie, and G. Radivoy, “Copper Nanoparticles in Click Chemistry,” *Acc Chem Res*, vol. 48, no. 9, pp. 2516–2528, Sep. 2015, doi: 10.1021/acs.accounts.5b00293.

[59] J. Idiago-López *et al.*, “From Bench to Cell: A Roadmap for Assessing the Bioorthogonal ‘click’ Reactivity of Magnetic Nanoparticles for Cell Surface Engineering,” *Bioconjug Chem*, vol. 33, no. 9, pp. 1620–1633, Sep. 2022, doi: 10.1021/acs.bioconjchem.2c00230.

[60] A. Lamoot, A. Uvyn, S. Kasmi, and B. G. De Geest, “Covalent Cell Surface Conjugation of Nanoparticles by a Combination of Metabolic Labeling and Click Chemistry,” *Angewandte Chemie - International Edition*, vol. 60, no. 12, pp. 6320–6325, Mar. 2021, doi: 10.1002/anie.202015625.

[61] S. M. M. Dadfar, S. Sekula-Neuner, U. Bog, V. Trouillet, and M. Hirtz, “Site-specific surface functionalization via microchannel cantilever spotting (µCS): Comparison between Azide–alkyne and thiol–alkyne click chemistry reactions,” *Small*, vol. 14, no. 21, May 2018, doi: 10.1002/smll.201800131.

[62] O. Paulino Da Silva Filho *et al.*, “A comparison of acyl-moieties for noncovalent functionalization of PLGA and PEG-PLGA nanoparticles with a cell-penetrating peptide,” *RSC Adv*, vol. 11, no. 57, pp. 36116–36124, Oct. 2021, doi: 10.1039/d1ra05871a.

[63] A. Harguindey *et al.*, “Click Nucleic Acid Mediated Loading of Prodrug Activating Enzymes in PEG-PLGA Nanoparticles for Combination Chemotherapy Graphical Abstract”, doi: 10.1021/acs.bio-mac.9b00040.

[64] V. Bouvet, M. Wuest, and F. Wuest, “Copper-free click chemistry with the short-lived positron emitter fluorine-18,” *Org Biomol Chem*, vol. 9, no. 21, pp. 7393–7399, Nov. 2011, doi: 10.1039/c1ob06034a.

[65] D. E. Lee *et al.*, “Facile method to radiolabel glycol chitosan nanoparticles with 64Cu via copper-free click chemistry for MicroPET imaging,” *Mol Pharm*, vol. 10, no. 6, pp. 2190–2198, Jun. 2013, doi: 10.1021/mp300601r.

[66] D. Svatunek *et al.*, “Live Monitoring of Strain-Promoted Azide Alkyne Cycloadditions in Complex Reaction Environments by Inline ATR-IR Spectroscopy,” *Chemistry - A European Journal*, vol. 26, no. 44, pp. 9851–9854, Aug. 2020, doi: 10.1002/chem.201905478.

[67] H. S. Min *et al.*, “Tuned Density of Anti-Tissue Factor Antibody Fragment onto siRNA-Loaded Polyion Complex Micelles for Optimizing Targetability into Pancreatic Cancer Cells,” *Biomacromolecules*, vol. 19, no. 6, pp. 2320–2329, Jun. 2018, doi: 10.1021/acs.biomac.8b00507.

[68] H. Wang *et al.*, “In vivo targeting of metabolically labeled cancers with ultra-small silica nanoconjugates,” *Theranostics*, vol. 6, no. 9, pp. 1467–1476, 2016, doi: 10.7150/thno.16003.

[69] J. Zhang *et al.*, “Systematic investigation on the intracellular trafficking network of polymeric nanoparticles,” *Nanoscale*, vol. 9, no. 9, pp. 3269–3282, Mar. 2017, doi: 10.1039/c7nr00532f.

[70] T. Zhao *et al.*, “Effects of fulvic acid on aggregation, sedimentation, and adsorption of Fe3O4 magnetic nanoparticles,” *Environmental Science and Pollution Research*, vol. 26, no. 21, pp. 21463–21474, Jul. 2019, doi: 10.1007/s11356-019-05441-2.

[71] K. Nwe and M. W. Brechbiel, “Growing Applications of ‘“Click Chemistry”’ for Bioconjugation in Contemporary Biomedical Research.”

[72] G. C. Tron, T. Pirali, R. A. Billington, P. L. Canonico, G. Sorba, and A. A. Genazzani, “Click chemistry reactions in medicinal chemistry: Applications of the 1,3-dipolar cycloaddition between azides and alkynes,” Mar. 2008. doi: 10.1002/med.20107.

[73] N. Mukerjee and S. Sonar, “Signature of click chemistry in exosome modification for cancer therapeutic,” Aug. 01, 2024, *Blackwell Publishing*. doi: 10.1002/ctd2.335.

[74] L. Du, H. Qin, T. Ma, T. Zhang, and D. Xing, “Supporting Information In Vivo Imaging-Guided Photothermal/ Photoacoustic Synergistic Therapy with Bioorthogonal Metabolic Glycoengineering-Activated Tumor Targeting Nanoparticles.”

[75] R. Sharma *et al.*, “Functionalized Peptide-Based Nanoparticles for Targeted Cancer Nanotherapeutics: A State-of-the-Art Review,” Oct. 18, 2022, *American Chemical Society*. doi: 10.1021/acsomega.2c03974.

[76] P. W. Erickson, J. M. Fulcher, P. Spaltenstein, and M. S. Kay, “Traceless Click-Assisted Native Chemical Ligation Enabled by Protecting Dibenzocyclooctyne from Acid-Mediated Rearrangement with Copper(I),” *Bioconjug Chem*, vol. 32, no. 10, pp. 2233–2244, Oct. 2021, doi: 10.1021/acs.bioconjchem.1c00403.

[77] J. Lu, M. Shi, and M. S. Shoichet, “Click chemistry functionalized polymeric nanoparticles target corneal epithelial cells through RGD-cell surface receptors,” *Bioconjug Chem*, vol. 20, no. 1, pp. 87–94, 2009, doi: 10.1021/bc8003167.

[78] H. Yu, P. Zhou, M. Deng, and Z. Shang, “Indirect readout in protein-peptide recognition: A different story from classical biomolecular recognition,” *J Chem Inf Model*, vol. 54, no. 7, pp. 2022–2032, Jul. 2014, doi: 10.1021/ci5000246.

[79] R. Pola, A. Braunová, R. Laga, M. Pechar, and K. Ulbrich, “Click chemistry as a powerful and chemoselective tool for the attachment of targeting ligands to polymer drug carriers,” *Polym Chem*, vol. 5, no. 4, pp. 1340–1350, Feb. 2014, doi: 10.1039/c3py01376f.

[80] S. Florinas *et al.*, “A Nanoparticle Platform to Evaluate Bioconjugation and Receptor-Mediated Cell Uptake Using Cross-Linked Polyion Complex Micelles Bearing Antibody Fragments,” *Biomacromolecules*, vol. 17, no. 5, pp. 1818–1833, May 2016, doi: 10.1021/acs.biomac.6b00239.

[81] J. Osuofa and S. M. Husson, “Preparation of Protein A Membrane Adsorbers Using Strain-Promoted, Copper-Free Dibenzocyclooctyne (DBCO)-Azide Click Chemistry,” *Membranes (Basel)*, vol. 13, no. 10, Oct. 2023, doi: 10.3390/membranes13100824.

[82] S. B. Van Der Meer *et al.*, “Click Chemistry on the Surface of Ultrasmall Gold Nanoparticles (2 nm) for Covalent Ligand Attachment Followed by NMR Spectroscopy,” *Langmuir*, vol. 35, no. 22, pp. 7191–7204, Jun. 2019, doi: 10.1021/acs.langmuir.9b00295.

[83] K. L. A. Chan and S. G. Kazarian, “FT-IR spectroscopic imaging of reactions in multiphase flow in microfluidic channels,” *Anal Chem*, vol. 84, no. 9, pp. 4052–4056, May 2012, doi: 10.1021/ac300019m.

[84] J. Budhathoki-Uprety and B. M. Novak, “Synthesis of alkyne-functionalized helical polycarbodiimides and their ligation to small molecules using ‘click’ and Sonogashira reactions,” *Macromolecules*, vol. 44, no. 15, pp. 5947–5954, Aug. 2011, doi: 10.1021/ma200960e.

[85] V. Ganesh, V. S. Sudhir, T. Kundu, and S. Chandrasekaran, “10 years of click chemistry: Synthesis and applications of ferrocene-derived triazoles,” Oct. 04, 2011. doi: 10.1002/asia.201100408.

[86] M. T. Constantin and M. A. Beleaua, “Recent progress in apoptosis triggering facilitated by HeLa Studies,” Jun. 01, 2023, *Sciendo*. doi: 10.2478/amma-2023-0022.

[87] C. Xu, W. Liu, Y. Hu, W. Li, and W. Di, “Bioinspired tumor-homing nanoplatform for co-delivery of paclitaxel and siRNA-E7 to HPV-related cervical malignancies for synergistic therapy,” *Theranostics*, vol. 10, no. 7, pp. 3325–3339, 2020, doi: 10.7150/thno.41228.

[88] H. L. Ma *et al.*, “Multicellular tumor spheroids as an in vivo-like tumor model for three-dimensional imaging of chemotherapeutic and nano material cellular penetration,” *Mol Imaging*, vol. 11, no. 6, pp. 487–498, Nov. 2012, doi: 10.2310/7290.2012.00012.

[89] H. Yuan, A. M. Fales, and T. Vo-Dinh, “TAT peptide-functionalized gold nanostars: Enhanced intracellular delivery and efficient NIR photothermal therapy using ultralow irradiance,” *J Am Chem Soc*, vol. 134, no. 28, pp. 11358–11361, Jul. 2012, doi: 10.1021/ja304180y.

[90] C. Dalal and N. R. Jana, “Multivalency Effect of TAT-Peptide-Functionalized Nanoparticle in Cellular Endocytosis and Subcellular Trafficking,” *Journal of Physical Chemistry B*, vol. 121, no. 14, pp. 2942–2951, Apr. 2017, doi: 10.1021/acs.jpcb.6b12182.

[91] G. Ruan, A. Agrawal, A. I. Marcus, and S. Nie, “Imaging and tracking of Tat peptide-conjugated quantum dots in living cells: New insights into nanoparticle uptake, intracellular transport, and vesicle shedding,” *J Am Chem Soc*, vol. 129, no. 47, pp. 14759–14766, Nov. 2007, doi: 10.1021/ja074936k.

[92] S. G. Patel *et al.*, “Cell-penetrating peptide sequence and modification dependent uptake and subcellular distribution of green florescent protein in different cell lines,” *Sci Rep*, vol. 9, no. 1, Dec. 2019, doi: 10.1038/s41598-019-42456-8.

[93] F. Duchardt, M. Fotin-Mleczek, H. Schwarz, R. Fischer, and R. Brock, “A comprehensive model for the cellular uptake of cationic cell-penetrating peptides,” *Traffic*, vol. 8, no. 7, pp. 848–866, Jul. 2007, doi: 10.1111/j.1600-0854.2007.00572.x.

[94] P. M. Perrigue *et al.*, “Cellular uptake and retention studies of silica nanoparticles utilizing senescent fibroblasts,” *Sci Rep*, vol. 13, no. 1, Dec. 2023, doi: 10.1038/s41598-022-26979-1.

[95] X. Xing, X. He, J. Peng, K. Wang, and W. Tan, “Uptake of silica-coated nanoparticles by HeLa cells,” *J Nanosci Nanotechnol*, vol. 5, no. 10, pp. 1688–1693, 2005, doi: 10.1166/jnn.2005.199.

[96] J. P. Richard *et al.*, “Cell-penetrating peptides: A reevaluation of the mechanism of cellular uptake,” *Journal of Biological Chemistry*, vol. 278, no. 1, pp. 585–590, Jan. 2003, doi: 10.1074/jbc.M209548200.

[97] R. Lee, D. H. Jo, S. J. Chung, H. K. Na, J. H. Kim, and T. G. Lee, “Real-Time and label-free monitoring of nanoparticle cellular uptake using capacitance-based assays,” *Sci Rep*, vol. 6, Sep. 2016, doi: 10.1038/srep33668.

[98] T. Dos Santos, J. Varela, I. Lynch, A. Salvati, and K. A. Dawson, “Quantitative assessment of the comparative nanoparticle-uptake efficiency of a range of cell lines,” *Small*, vol. 7, no. 23, pp. 3341–3349, Dec. 2011, doi: 10.1002/smll.201101076.

[99] L. Leclerc *et al.*, “Quantification of microsized fluorescent particles phagocytosis to a better knowledge of toxicity mechanisms,” *Inhal Toxicol*, no. 13, pp. 1091–1100, 2010, doi: 10.3109/08958378.2010.522781ï.

[100] D. Van Der Zwaag, N. Vanparijs, S. Wijnands, R. De Rycke, B. G. De Geest, and L. Albertazzi, “Super Resolution Imaging of Nanoparticles Cellular Uptake and Trafficking,” *ACS Appl Mater Interfaces*, vol. 8, no. 10, pp. 6391–6399, Mar. 2016, doi: 10.1021/acsami.6b00811.

[101] A. Balfourier *et al.*, “Multiscale Multimodal Investigation of the Intratissural Biodistribution of Iron Nanotherapeutics with Single Cell Resolution Reveals Co-Localization with Endogenous Iron in Splenic Macrophages,” *Small Methods*, vol. 7, no. 2, Feb. 2023, doi: 10.1002/smtd.202201061.

[102] H. Peuschel, T. Ruckelshausen, C. Cavelius, and A. Kraegeloh, “Quantification of Internalized Silica Nanoparticles via STED Microscopy,” *Biomed Res Int*, vol. 2015, 2015, doi: 10.1155/2015/961208.

[103] A. D. Elliott, “Confocal Microscopy: Principles and Modern Practices,” *Curr Protoc Cytom*, vol. 92, no. 1, Mar. 2020, doi: 10.1002/cpcy.68.

[104] A. Mali *et al.*, “The internal structure of gadolinium and perfluorocarbon-loaded polymer nanoparticles affects 19F MRI relaxation times,” *Nanoscale*, vol. 15, no. 44, pp. 18068–18079, Oct. 2023, doi: 10.1039/d3nr04577c.

[105] A. M. Silva *et al.*, “In vitro cytotoxicity of oleanolic/ursolic acids-loaded in PLGA nanoparticles in different cell lines,” *Pharmaceutics*, vol. 11, no. 8, Aug. 2019, doi: 10.3390/pharmaceutics11080362.

[106] N. Yadav, A. K. Tripathi, A. Parveen, S. Parveen, and M. Banerjee, “PLGA-Quercetin Nano-Formulation Inhibits Cancer Progression via Mitochondrial Dependent Caspase-3,7 and Independent FoxO1 Activation with Concomitant PI3K/AKT Suppression,” *Pharmaceutics*, vol. 14, no. 7, Jul. 2022, doi: 10.3390/pharmaceutics14071326.

[107] M. H. M. Leung and A. Q. Shen, “Microfluidic Assisted Nanoprecipitation of PLGA Nanoparticles for Curcumin Delivery to Leukemia Jurkat Cells.”

Supplementary

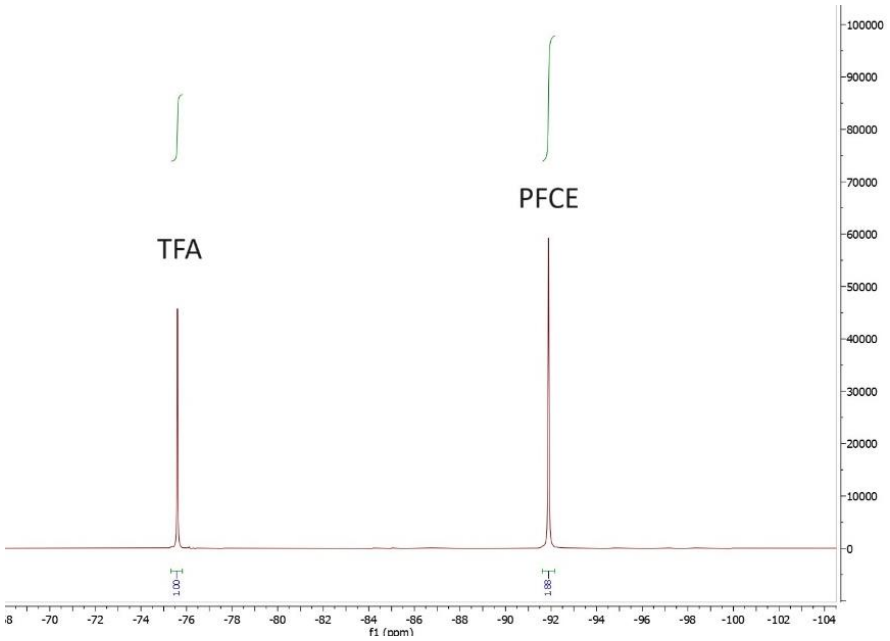

Figure 14:[19]*F NMR measurement of PLGA-PFCE NP, labeled for the PFCE peak and the TFA internal standard peak. The integrals for TFA and PFCE are 1.00 and 1.88.*

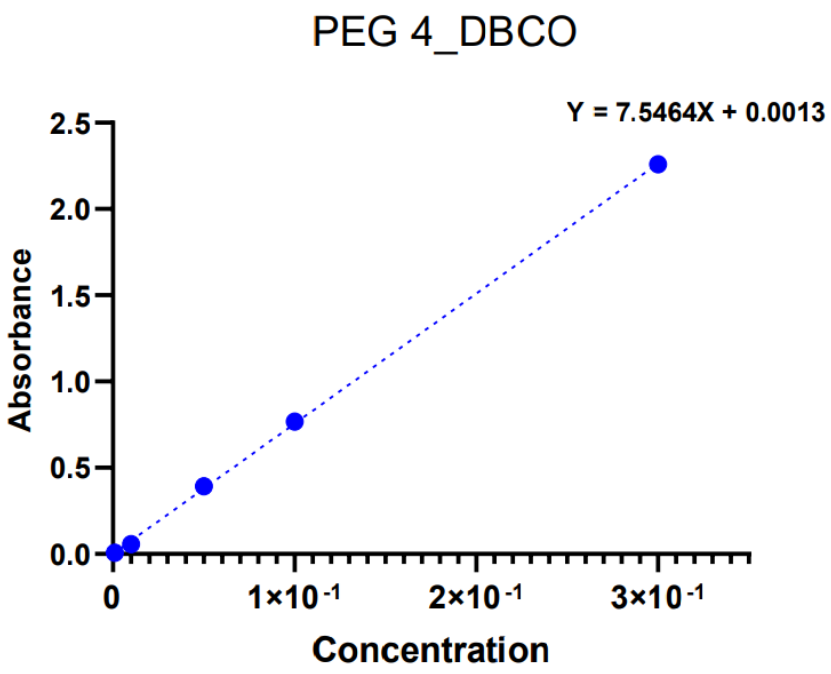

Figure 15: *Standard curved of PEG4-DBCO based on different concentration*